AN INTEGRATED PREDICTION MODEL FOR H_2S/CO_2 CORROSION IN THE PIPE OF REFINERY

A Thesis

by

LIHAN ZENG

Submitted to the Office of Graduate and Professional Studies of
Texas A&M University
in partial fulfillment of the requirements for the degree of

MASTER OF SCIENCE

Chair of Committee,	M. Sam Mannan
Committee Members,	Mahmoud M. El-Halwagi
	Eric L. Petersen
Head of Department,	M. Nazmul Karim

May 2017

Major Subject: Chemical Engineering

ABSTRACT

Corrosion of equipment is one of the most vital factors that results in serious process safety incidents. Though various types of equipment are subject to corrosion issues to different extent depending on the process conditions, the pipe and the piping network connecting units and equipment are relatively more vulnerable to corrosion. The vulnerability of a pipe to internal corrosion is predominantly due to the process conditions. Among the factors contributing to the internal corrosion, substances creating corrosive conditions in the pipe, such as CO_2 and H_2S, are the most common factors, followed by the flow condition of processes (flow rate and temperature). In this paper, a single-phase integrated prediction model for H_2S/CO_2 corrosion is developed to study a holistic effect of most important variables. The model investigates the electrochemical kinetics of corrosive substances, the scale formation conditions, and the flow conditions that have impact on the mass transport of corrosive species. The COMSOL software based on finite element method is used to simulate all these. The prediction results of present model are in good accordance with the measured field data. Additionally, it is found in the present model that the charge transfer current density has significant contribution to the corrosion rate, which is ignored in some other models. Apart from that, other comparisons have been made to investigate the impact on corrosion rate as a function of flow region, H_2S and CO_2 concentration, and temperature. Finally, the present model is able to provide the information on if there are FeS (or $FeCO_3$) protective scales formed at steel surface.

DEDICATION

This Thesis is dedicated to

my parents, Zhong Zeng and Liyi Li

and

my loved Yan Cui

ACKNOWLEDGEMENTS

I would like to express my deepest appreciation to my advisor, Dr. M. Sam Mannan for his excellent guidance, caring, patience, and providing me with a unique atmosphere for doing research with him.

I would also like to thank my committee members, Dr. Mahmoud M. El-Halwagi, Dr. Chad V. Mashuga and Dr. Eric L. Petersen for their precious comments and suggestions on my research projects and the scientific thinking.

Thanks also go to my friends and colleagues and the department faculty and staff for making my time at Texas A&M University a great experience. Finally, thanks to my girlfriend for her encouragement, patience and love.

CONTRIBUTORS AND FUNDING SOURCES

Contributors

Part 1, faculty committee recognition

This work was supervised by a thesis committee consisting of Professor M. Sam Mannan and Professor Mahmoud M. El-Halwagi of the Department of Chemical Engineering and Professor Eric L. Petersen of the Department of Mechanical Engineering.

Part 2, student/collaborator contributions

All work for the thesis was completed independently by the student.

Funding Sources

There are no outside funding contributions to acknowledge related to the research and compilation of this document.

TABLE OF CONTENTS

LIST OF FIGURES

Page

LIST OF TABLES

Page

CHAPTER I

INTRODUCTION

1.1 Background

Oil refining industry has been playing a significant role in global economy development. Not only is the source of energy for transportation and residential use dependent on the refined products, but also the manufactory industry that largely consumes the petrochemicals relies on the oil refining industry, since the refined products are the feedstocks of various industry products as well as consuming goods such as resins, plastics, engineering materials and fibers. Due to the influence on the downstream manufactory to a large extent, the existence of refinery sector is not only the strategic advantage in a single country or region, but in a global-wide range.

Corrosion of an equipment part is one of the most important factors that results in the serious process safety incidents in oil & gas industry. The reliability of equipment can reduce gradually till the serious failure due the uncontrolled corrosion that results in the release of hazardous materials. Therefore, corrosion can put plant personnel and production at risk, which can lead to the damage or even shutdown of the units.

Although different types of equipment can be subject to corrosion issues to different extent depending on the process conditions, the pipe and the pipe network connecting units and equipment are relatively more vulnerable to corrosion. The

vulnerability of pipe to corrosion is due to the internal process conditions. According to the study by JCS in 2013 [1], it has been identified what types of substances and operation conditions were the major contributors that lead to corrosion associated incidents, among which substance was the biggest contributor and the following was the flow conditions.

Crude oil and natural gas can carry many high-impurity products which are inherently corrosive. Among those impurities, the most common ones are CO_2 and H_2S, which can cause sweet corrosion and sour corrosion in the presence of free water in oil and gas pipes. CO_2 corrosion, or sweet corrosion, has been a recognized problem in oil and gas production and transportation facilities for many years due to the technique of CO_2 injection for enhanced oil recovery. CO_2 is one of the main corroding agents in the oil and gas production systems. Dry CO_2 gas itself is not corrosive within oil and gas production systems but is corrosive when mixed with free water. The corrosion of metal due to contact with hydrogen sulfide (H_2S) and moisture is called sour corrosion which is the most damaging corrosion to pipe. Although H_2S is not corrosive by itself as well, it becomes severely corrosive in the presence of water.

1.2 Corrosion associated incidents in oil refining industry

Since 1984, around 20% corrosion failures were reported as an important contributing factor in 137 major refinery accidents in EU countries[1]. And in the U.S, the

cost related to corrosion in the oil industry has been estimated about $3.7 billion per year[1].

On August 6, 2012, the Chevron Richmond Refinery in California experienced a catastrophic pipe rupture and fire incident. The incident was caused by a pipe rupture on a 52-inch long component due sulfidation corrosion. At the time of the incident, light gas oil was flowing through the 8-inch line at a rate of approximately 10,800 barrels per day (bpd). During the weeks after the incident, it was estimated that local hospitals received over 15,000 people of the public who sought treatment for ailments [2].

Chevron Richmond Refinery incident in 2012 was not the first one that was caused by sulfidation corrosion at a Chevron refinery. In 1988, a low silicon carbon steel (0.02 wt. % silicon) piping component failed at the Chevron's former El Paso Refinery in El Paso, Texas. In addition, in 2002, a fire incident occurred at the Chevron Salt Lake City Refinery which was caused by a process piping failure because of sulfidation corrosion in a carbon steel pipe, where the corrosion rate was failed to be detected at the rupture location. Compared with the corrosion rates at other locations in the pipe that were successfully detected, the corrosion rate at the failure point was estimated to be five times greater. It has been realized in the following incident investigation that the increase in operation temperature and concentration hydrogen sulfide over time was the major contributor that increased the corrosion rate and final rupture [2].

On November 9, 2009, the Silver Eagle refinery in Woods Cross, Utah, experienced a severe pipe rupture and fire incident due to sulfidation corrosion in the pipe.

The corrosion rate also increased because of the temporarily increased temperature that was higher than the regular operational temperature. The ruptured pipe located on the bottom of a dewaxing reactor released hydrogen, which then led to fire and explosion. The consequences of incidents included injuries of four workers and damages on over 100 homes in the near neighborhood [2].

On October 6, 2011, Canadian refinery in Regina, Saskatchewan experienced a pipe rupture due to hydrogen sulfide corrosion, which then resulted in a catastrophic explosion and fire incident, where 52 workers were injured. Although the company's detection data showed the wall thickness of overall piping system in the refinery was within acceptable range, corrosion rate at the failure location was higher than other locations and was not correctly inspected [2].

1.3 Corrosion prediction models

Corrosion can cause severe incidents with fires and fatalities in a refinery unit, since corrosion is ubiquitous. Therefore, the chance of failures such as ruptures or large leaks due to corrosion is higher than pinhole leaks due to human error. Because of difficulties in detecting high corrosion rate and the change of process conditions such as the increase in flow rate and temperature that can facilitate the corrosion rates over time, equipment failure due to corrosion always takes place before the increased corrosion rate is detected.

So corrosion prediction models are largely utilized to help corrosion engineers and scientists for the decision-making process when designing an oil & gas production (or treatment) facility and scheduling the mechanical integrity inspection, which involves the use of corrosion resistant alloys (CRA) that is with high economic cost, corrosion inhibitor as well as other mitigation approaches. Corrosion predictions models can be divided into two types: empirical model versus mechanistic model. The empirical models are dependent mostly on the empirical correlations with experimental results or field data, while the mechanistic models are mainly based on the first principle derivation of chemical/ electrochemical reaction and transport phenomena involved in a corrosion process, although some experimental data are needed to adjust and calibrate the models. One major contrast that differentiates a mechanistic model from an empirical one is that the mechanistic model is able to predict the formation and protective effect of corrosion scales. The related corrosion mechanisms that a corrosion prediction model may consider includes: kinetics of electrochemical reactions on metal surface, homogeneous reaction of corrosive species, formation of protective scales, mass transport as well as flow conditions and flow regime, etc. Not all the models include all these factors, and models with different approach to have different emphasis on treating various factors and parameters.

All models have limitations since they are developed for the application with respect to specific environmental conditions and certain systems. Thus, all the prediction models applied for a specific condition should be verified by experimental or field data under the same condition. Therefore, the empirical models have the advantage of utilizing ranges of data that they correlate with. For example, as shown in Table 1, different oil

companies and research institutions have developed models to predict H_2S/CO_2 corrosion in carbon steel pipe, most of which are empirical or semi-empirical models. Those models work well for the worst-case scenario, but varies widely when more complex effects are considered, such as the formation and growth of protective scales. This is because that the empirical models largely rely on the empirical correction factors when dealing with complex effects under specific corrosion environment.

Table 1. Corrosion prediction models developed by different oil & gas companies

Model	Developer	Year	Description
De Waard	Shell	1995	Uses a scale factor to take account for corrosion product scales
Cassandra	BP	1997	De Waard model including BP's experience in using this model
Lipucor	Total	1996	Based on both laboratory results and a large amount of field data
Hydrocor	Shell	2002	Combines corrosion and fluid flow modeling

Similarly, mechanistic models also need verification from large number of data in order to be applicable for the more accurate prediction within the range of data. The corrosion mechanisms that a corrosion prediction model may consider mentioned in the previous paragraph have been intensively studied in the past three decades, with some CO_2 corrosion model being developed [3-8]. These models are able to predict very well in the case of no protective scale formation, while the deviation is obvious in the presence of iron carbonate scale which is formed from CO_2 corrosion.

Different from CO_2 corrosion, H_2S corrosion mechanism is more complex, which means the prediction is more difficult to achieve, since the understanding in H_2S corrosion mechanism is insufficient, and the research papers studying the electrochemical reaction of hydrogen sulfide and the formation of iron sulfide scale are limited [9-13].

1.4 Research objectives

In this research, a mechanistic H_2S/CO_2 corrosion model is developed that integrates the effect of most important variables including kinetics of electrochemical reaction involving corrosive substances, protective scale effects, and effect of flow conditions on the mass transport of corrosive species.

As shown in Scheme 1, the first part of model is to study the electrochemical reaction on the steel surface. Since the corrosion process is electrochemical in nature, the corrosion rate can be determined by calculating the rate of the electrochemical reaction, which is the kinetics of the reaction: such as oxidation of iron (anodic reaction) and the reduction of acid (cathodic reaction). The electrochemical reaction rate can be expressed as current density, which is a function of the reaction potential, while the potential is an important measure of thermodynamics to show which specie can react or react first. So in this part of process, it is necessary to investigate how the reaction conditions like pH, temperature and concentration will affect the thermodynamics and kinetics of the corrosion reaction on the steel surface.

Once the corrosion reaction takes place, the formation of corrosion product may occur, depending on the saturation of corrosion products, and this step is called scale formation. When the corrosion products precipitate at the steel surface, which it could be either iron carbonate or iron sulfide, or both, it can slow down the corrosion process by providing a diffusion barrier. However, depending on different solution conditions, like pH and temperature the composition and thickness of scale can be different, which will have different effect on corrosion rate. This because the porosity of iron sulfide and iron carbonate are different, which have different effect on the mass transport of corrosive species.

Another important factor that affects the corrosion rate is the flow condition. The flow condition will affect the mass transport efficiency of corrosive species in the boundary layer, since the flow condition will determine the distribution of velocity and turbulent kinetic energy, which will have the influence on the mass transport coefficient and the mechanical damage on protective scales.

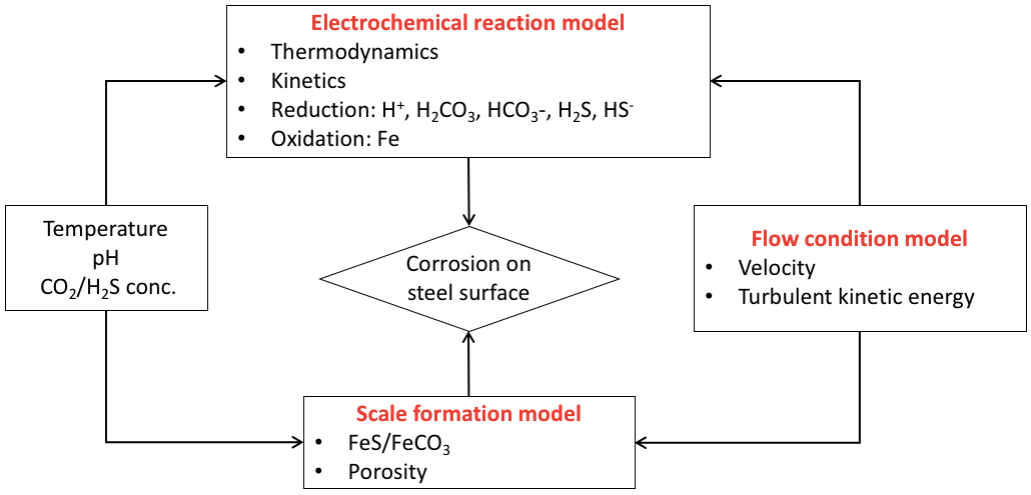

Scheme 1. Framework of integrated mechanistic H_2S/CO_2 corrosion prediction model

1.5 Outline of research in this thesis

A general literature review and extension of the theory behind H_2S/CO_2 corrosion is presented in Chapter 2. First of all, the basic kinetics of corrosion reaction is presented, which includes the water chemistry and the electrochemical reaction on carbon steel surface. Second, the theory and general description of mass transport of corrosive materials is demonstrated such as Nernst-Planck equation and effects of flow. In the following part of literature review, the development and the mechanism of mechanistic models for H_2S/CO_2 corrosion prediction in the publications are described and explained, with some key chemical reactions and empirical equations for the equilibrium constants being listed. These prediction model in this literature reviews are electrochemical reaction model, mass transport model and scale formation model.

The development of H_2S/CO_2 corrosion prediction model in this research work is described in Chapter 3. Based on the existed models in the literature review in Chapter 2, some of the models will be modified and included with factors that are not considered in the existed models. Then the models associated with electrochemical reaction, mass transport and scale formation are "connected" together to form a one-dimensional integrated corrosion model. In the last part of Chapter 3, the one-dimensional integrated corrosion model is coupled with a three-dimensional flow field & regime model to give a

completed H_2S/CO_2 corrosion prediction model that can generate a "map" of corrosion rate distribution at different flow regime.

The results of developed corrosion model as well as the comparison with experimental data in open publications are discussed in Chapter 4. Conclusion and suggestion for future work are presented in chapter 5 and 6.

CHAPTER II

LITERATURE REVIEW

2.1 Electrochemical corrosion theory

Uniform corrosion is basically the electrochemical corrosion, which is sustained by a current flow in a short-circuited electrochemical cell, and this is also the basis of many other corrosion mechanisms such as crevice corrosion, intergranular corrosion and pitting corrosion. In this section, the basic principles of electrochemical kinetics of corrosion reaction is presented in the following parts.

2.1.1 Polarization Resistance

Stern and Geary have developed a fundamental theory for polarization resistance in 1950s [14]. In a corroding system, there are two or more co-existing half-cell electrochemical reactions conducting electrons via the short-circuit in solution. The oxidation reaction of metal losing electrons takes place at the anode:

$$M \rightarrow M^{+} + e^{-} \tag{1}$$

The other half-cell electrochemical reaction is the reduction of a corrosive specie in the solution at the cathode:

$$Z^{+} + e^{-} \rightarrow Z \tag{2}$$

The equilibration potentials of the couples in equations (1) and (2) are labeled $E_{eq,M}$ and $E_{eq,Z}$, respectively. The corrosion potential (E_{corr}) is the potential at which the current density of oxidation reaction at anode ($i_{ox,M}$) is equal to current density of reduction reaction at cathode ($i_{red,Z}$). Since the electrochemical reaction rate is proportional to current density, the reaction rate of cathode and anode reaches equilibrium at corrosion potential. Also, the difference between the current density of cathode and anode is called net current, which is measured to be zero with an external device.

$$i_{meas} = i_{ox,M} - i_{red,Z} = 0 \tag{3}$$

$$i_{corr} = i_{ox,M} = i_{red,Z} \tag{4}$$

Here i_{corr} is directly related with the corrosion rate of metal, which will be elaborated in the later part.

2.1.2 Tafel Plots

A Tafel plot is obtained by polarizing the metal within the potential range of $\pm$300 mV from the corrosion potential, E_{corr}. The potential applied to metal for polarization can either be continuously scanned or step wised. An example of experimentally obtained Tafel plot is as shown in Figure 1.

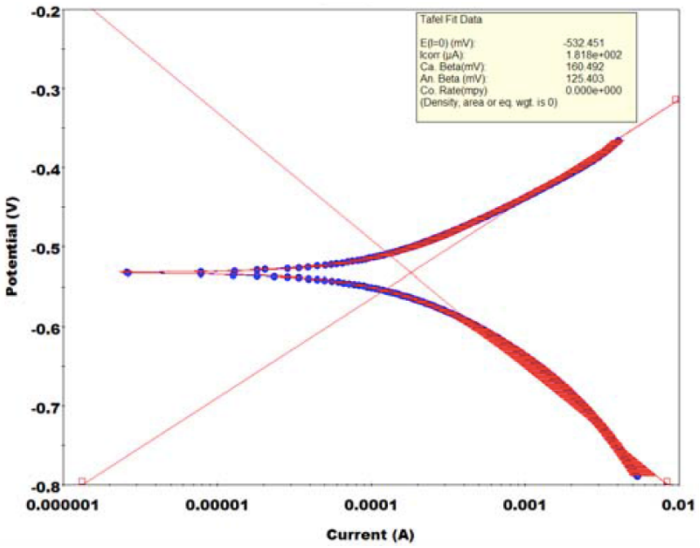

Figure 1. Example of experimentally measured Tafel plot [15].

The logarithmic Tafel plot can be expressed by the Tafel equation for both anode and cathode, where η is the over potential (the difference between the applied potential E and corrosion potential E_{corr}), β_A and β_C are Tafel constants for anode and cathode, respectively, i is the current in μA at applied potential E. It can be noticed from the Equation (5) or (6) that when the applied potential (E) is equal to the corrosion potential E_{corr} ($\eta = 0$), the current i at the applied potential is equal to the i_{corr}.

$$\eta = \beta_A log\left(\frac{i_{ox,M}}{i_{corr}}\right) \tag{5}$$

$$\eta = \beta_C log\left(\frac{i_{red,Z}}{i_{corr}}\right) \tag{6}$$

Making rearrangement on Equation (5) or (6) can give Equation (7), which make η have a linear correlation with log(i) in forms of y=kx+b. And the slope of the new plot

is the Tafel constant β. Therefore, the Tafel constant can be determined from the plot of experimental data.

$$\eta = \beta[log(i) - log\ (i_{corr})] \tag{7}$$

2.1.3 Calculation of corrosion rate from current density

As is shown the Faraday's Law in Equation (8), Q is coulomb number, n is the number electrons transferred in the electrochemical reaction at electrode surface, F is Faraday constant (F=96,478), W is the weight of electroactive species, and M is molecular weight.

$$Q = \frac{nFW}{M} \tag{8}$$

By knowing Q=I*t (t is time) and defining equivalent weight (E.W.) is the ratio of M/n, rearrange Equation (8) to get:

$$\frac{W}{t} = \frac{I(E.W.)}{F} \tag{9}$$

Here W/t is the corrosion rate with in forms of grams per second. However, the corrosion rate (CR) is normally expressed with the unit mm/year. So by dividing Equation (9) on both sides with the corrosion area A and the metal density ρ and converting time scale from second to year, we are able to obtain the expression for CR in terms of mm/year (Equation (10)), where i is current density (A/m^2) at electrode (or metal) surface, (E.W.) is equivalent weight of metal (g) and ρ_M is density of corroding metal, (g/m^3).

$$CR(mm/yr) = \frac{32.68 * i * (E.W.)}{\rho_M} \quad (10)$$

2.2 Water chemistry

2.2.1 Water chemistry of CO_2

Since the pipes transporting oil & gas products always carry some amount of CO_2 gas and water as the same time. When CO_2 gas dissolves in water, a series of chemical reactions (see Table 2) will occur, which include the formation and dissociation of H_2CO_3. These basic chemical reaction equations determine the equilibrium and concentration of different carbonic species under different solution conditions that will further determine the corrosion rate at the metal surface [4, 16, 17]. The calculation of relevant equilibrium constants is listed in Table 3.

Table 2. Chemical reactions of CO_2 in aqueous solution and relevant reaction equilibrium equations

Reaction name	Reaction equation		Equilibrium equation	
CO_2 dissolution	$CO_{2(g)} \rightleftharpoons CO_{2(aq)}$	(11)	$K_{sol} = \frac{c_{CO_2}}{p_{CO_2}}$	(12)
CO_2 hydration	$CO_{2(aq)} + H_2O \rightleftharpoons H_2CO_{3(aq)}$	(13)	$K_{hyd} = \frac{c_{H_2CO_3}}{c_{CO_2}}$	(14)

Reaction name	Reaction equation		Equilibrium equation	
H_2CO_3 dissociation	$H_2CO_{3(aq)} \rightleftharpoons H^+_{(aq)} + HCO^-_{3(aq)}$	(15)	$K_{ca} = \frac{C_{HCO_3^-} C_{H^+}}{C_{H_2CO_3}}$	(16)
HCO_3^- dissociation	$HCO_3^- \rightleftharpoons H^+_{(aq)} + CO^{2-}_{3(aq)}$	(17)	$K_{bi} = \frac{C_{CO_3^{2-}} C_{H^+}}{C_{HCO_3^-}}$	(18)
H_2O dissociation	$H_2O \rightleftharpoons H^+_{(aq)} + OH^-_{(aq)}$	(19)	$K_{wa} = C_{H^+} C_{OH^-}$	(20)

Table 3. Equations for the equilibrium constant calculation for CO2

Equilibrium constant			Source
$K_{sol} = \frac{14.5}{1.00258} \times 10^{-\left(2.27+5.65\times10^{-3}T_f - 8.06\times10^{-6}T_f^2 + 0.075I\right)}$	(mol/bar)	(21)	[18]
$K_{sol} = 2.58 \times 10^{-3}$		(22)	[19]
$K_{ca} = 387.6\times10^{-\left(6.41-1.594\times10^{-3}T_f + 3.52\times10^{-6}T_f^2 - 3.07\times10^{-5}p - 0.47721I^{0.5} + 0.11807I\right)}$	(mol)	(23)	[18]
$K_{bi} = 10^{-\left(10.61-4.97\times10^{-3}T_f + 1.331\times10^{-5}T_f^2 - 2.624\times10^{-5}p - 1.66I^{0.5} + 0.34661I\right)}$	(mol)	(24)	[18]
$K_{wa} = 10^{-\left(29.3868 - 0.0737549T_k + 7.47881\times10^{-5}T_k^2\right)}$	(mol^2)	(25)	[20]

*T_f is temperature in °F, T_k is absolute temperature in K, I is ionic strength in molar: $I = \frac{1}{2}\sum_i C_i Z_i^2$, and p is the pressure in bar

To calculate the bulk concentration of different carbonic species and protons in an aqueous solution, a water chemistry model needs to be developed. In the aqueous solution, the concentrations of six species need to determine which are CO_2, H_2CO_3, HCO_3^-, CO_3^{2-}, OH^- and H^+, while there are only 5 equations available (see Table 2). Due to the electro-neutrality of the solution, the number of negative charges should be equal to the number of positive charge. Therefore, the sixth equation (Equation (26)) is found to solve the concentration of six species.

$$C_{H^+} = C_{HCO_3^-} + 2C_{CO_3^{2-}} + C_{OH^-} \quad (26)$$

Here the expression in Equation (26) only considers the condition with pure CO_2 If in the case with other ions in the solution such as Fe^{2+}, HS^- and S^{2-}, etc., Equation (26) should be modified with regard to the change of charged species in the solution. In addition, the equilibrium equations listed in Table 2 should be modified or added for the new species (e.g., H_2S) that will be involved in the homogeneous reactions.

From what have been discussed above, CO_2 partial pressure contributes to change in pH value of the solution, which decreases as CO_2 partial pressure increases. H_2CO_3 formed from CO_2 dissolution is not only a corroding specie itself that can react at the metal surface, but also the acidic agent by giving hydrogen ions from carbonic acid dissociation. Since the hydrogen ion are also the corrosive specie for the cathodic reaction, the decrease of pH value in the solution can facilitate the corrosion process. Since pH and CO_2 pressure have influence on the equilibrium of H_2CO_3 dissociation and the concentration of CO_3^{2-}, both factors will affect the formation of iron carbonate, which plays a role protective scale, because, as shown in Equation (27) the saturation of iron carbonate is determined by the concentration of CO_3^{2-} [21].

$$S_{FeCO_3} = \frac{C_{Fe^{2+}} C_{CO_3^{2-}}}{K_{spFeCO_3}} \quad (27)$$

where K_{spFeCO_3} is the solubility product of iron carbonate.

In summary, CO_2 plays an important role in affecting the water chemistry and pH of solution, which will further impact the electrochemical reaction at metal surface as well as the formation of protective scales.

2.2.2 Water chemistry of H_2S

Similar to the properties of CO_2, H_2S can be treated as a weak acid in aqueous solutions and can partially dissociate to give hydrogen ions. If both the concentration of H_2S in aqueous phase and the H_2S partial pressure are low enough, Henry's law can be applied to calculate the solubility of H_2S. The chemical reactions of H_2S occurring in the bulk solution and metal surface and related equilibrium equations are listed in Table 4. Extensive research work has been done to investigate the thermodynamics of H_2S reactions in aqueous solution [22]. Major equations for the equilibrium constant calculation that will be used in this thesis are listed in Table 5.

Table 4. Chemical reactions of H_2S in aqueous solution and relevant reaction equilibrium equations

Reaction name	Reaction equation		Equilibrium equation	
H_2S dissolution	$H_2S_{(g)} \rightleftharpoons H_2S_{(aq)}$	(28)	$K_{sol} = \frac{c_{H_2S}}{p_{H_2S}}$	(29)
H_2S dissociation	$H_2S_{(aq)} \rightleftharpoons H^+_{(aq)} + HS^-_{(aq)}$	(30)	$K_{hs} = \frac{c_{HS^-} c_{H^+}}{c_{H_2S}}$	(31)
HS^- dissociation	$HS^-_{(aq)} \rightleftharpoons H^+_{(aq)} + S^{2-}_{(aq)}$	(32)	$K_{bi} = \frac{c_{S^{2-}} c_{H^+}}{c_{HS^-}}$	(33)

Table 5. Equations for the equilibrium constant calculation for H_2S

Equilibrium constant			Source
$K_{sol_{(H_2S)}} = 10^{-\left(634.27+0.2709T_k-0.00011132T_k^2-16719/T_k-261.9log\,(T_k)\right)}$	(mol/bar)	(34)	[23]
$K_{hs} = 10^{\left(782.43945-0.36126T_k-0.00016722T_k^2-20565.7315T_k-142.7417222log\,(T_k)\right)}$	(mol)	(35)	[23]
$K_{bs} = 10^{\left(-23.93+0.030446T_k-2.4831\times10^{-5}T_k^2\right)}$	(mol)	(36)	[20]

* T_k is absolute temperature in K

The way to calculate the concentrations of sulfide species involved in the reactions listed in Table 4 is similar to that of pure CO_2. Different from the case of CO_2, 5 different sulfide species are with unknown concentrations which are H^+, OH^-, H_2S, HS^- and S^{2-}, while there are only 4 equations available in Table 4. Again, one more electro-neutrality equation (Equation (37)) is needed to solve the concentration of all the sulfide species.

$$C_{H^+} = C_{HS^-} + 2C_{S^{2-}} + C_{OH^-} \tag{37}$$

By comparing the equations in Table 2 and Table 4, it can be indicated that one major difference of H_2S water chemistry from CO_2 is that H_2S can directly form the weak acid in the aqueous solution with a single step, while the formation of H_2CO_3 involves two steps: dissolution and hydration. Thus, the corresponding calculations for concentrations of H_2S and H_2CO_3 are $C_{H_2S} = K_{sol_{(H_2S)}} p_{H_2S}$ and $C_{H_2CO_3} = K_{sol} K_{hyd} p_{CO_2}$, respectively.

2.3 Mass transport of electrolyte

2.3.1 The volumetric component mass balance

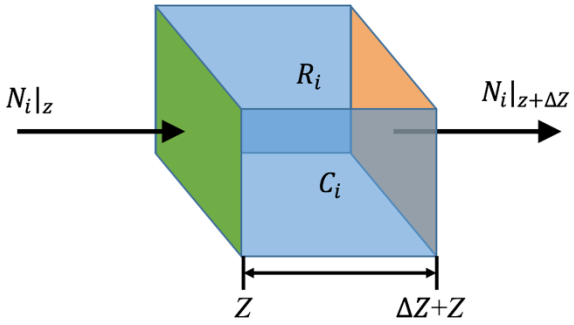

Figure 2. Mass balance in a controlled volume

The mass balance across the section area A (m^2) of a controlled volume (as shown in Figure 2), where $V = A \cdot \Delta Z$ (m^3) and length ΔZ (m) of component i is given by equation (38). The left side of mass balance equation are the terms of molar flux in, $N_i|_{\Delta Z}$ (mol/(m^2s)), and mass generation (or consumption) by chemical reaction, R_i (mol/(m^3s)). The right side are the flux out, $N_i|_{z+\Delta Z}$ and the overtime, Δt (s), accumulation of concentration, C_i (mol/m^3):

$$(\Delta t \cdot A \cdot N_i)|_Z + \Delta t \cdot R_i \cdot V = (\Delta t \cdot A \cdot N_i)|_{Z+\Delta Z} + (C_i|_{t+\Delta t} - C_i|_t)V \qquad (38)$$

The direction of both flux, $N_i|_Z$ and $N_i|_{Z+\Delta Z}$, are perpendicular to the section plane A. Dividing Equation (38) by $A\Delta t\Delta Z$ ($\Delta Z \to 0$ and $\Delta t \to 0$) and rearranging the terms, we

can obtain a mass balance equation in terms partial differential equation (PDE) as shown in Equation (39):

$$\frac{\partial C_i}{\partial t} = \frac{\partial N_i}{\partial z} + R_i \tag{39}$$

As for the three dimensional case, Equation (39) can be rewritten as

$$\frac{\partial C_i}{\partial t} = \nabla \cdot N_i + R_i \tag{40}$$

$$\nabla \cdot N_i = \frac{\partial N_{i,x}}{\partial x} + \frac{\partial N_{i,y}}{\partial y} + \frac{\partial N_{i,z}}{\partial z} \tag{41}$$

2.3.2 The use of Nernst-Planck equation in mass transport

In order to correctly describe the mass transport of electrolyte in solutions, the Nernst-Planck equation is useful obtain to a more comprehensive description. In most cases, the Nernst-Planck equation is suitable for dilute solutions. However, for concentrated solutions, some assumptions are necessary to be made to deal with the effect of ionic strength in the solution. The general form of Nernst-Planck equation is expressed in Equation (42):

$$\frac{\partial C_i}{\partial t} = \nabla \cdot (D_i \nabla C_i) + \frac{z_i F}{RT} \nabla \cdot (D_i C_i \nabla \Phi) - \nabla \cdot (C_i v) + R_i \tag{42}$$

where C_i is the concentration of corrosive species i, D_i is the diffusion coefficient of species i, z_i is the number of charges of species i, F is Faraday's constant, Φ is the electric potential, v is the fluid velocity, and R_i is rate of homogeneous chemical reactions generating (or consuming) species i.

The term on the left side of equation is the concentration change overtime; the first twos terms on the right side is the diffusion of corrosive species from bulk solution to metal surface, and the migration induced by the induced potential gradient. The third term is the mass transfer due to the convection of fluid. In general, the convection term is neglected in the boundary layer mass transport in corrosion modeling, although the research done by Harb and Alkire indicated that convection should be considered when dealing with the mass transport at the entrance of a pit [24].

Another assumption in modeling of mass transport in a corrosion system is electro-neutrality. Electro-neutrality states that any volume of solution is electrically neutral due to the large restoring force resulting from any separation of charge [25]. The solution to the Nernst-Planck equation gives full transient profiles of the distributions of species concentration, potential, and current density. However, in general, it is also assumed that the solution does not transport current in the diffusion boundary layer which can simplify the modeling by avoiding the difficulties in calculating the potential gradient.

The difficulties in solving this differential equation are computational convolution and time. The corrosion modeling involves various types of processes, which are so different from each other in time scales. For example, the electrochemical reactions on metal surface and the homogeneous chemical reactions in solutions are very fast when compared with slow processes such as mass transfer in the diffusion boundary layer. In addition to the problems of different timescales, the nonlinear boundary conditions such as kinetics of electrochemical reactions that will be used to “connect” the models together

can also bring in more difficulties for calculation. So this requires very small time steps and highly refined spatial meshing, which will inevitably increase the computational time.

2.3.3 Effect of flows

As mentioned in Chapter 1, flow features have significant impact on the mass transfer of corrosive species in the boundary layer and the corrosion rate. Especially, when the flow rate increases or there is a turbulent flow, the corrosion rate can be accelerated because the flow can change the patterns of diffusion boundary layer, which enhance the mass transport of corrosive species from bulk solutions to the metal surface.

For example, when the corrosion system is absent of protective scales formed from corrosion product, the H_2S induced corrosion rate is readily to sensitive to the flow rate, since, as mentioned in section 2.2, H_2S can immediately and partially dissociate to hydrogen ions once being dissolved, and the reduction of hydrogen ion is mass transfer controlled. In contrast, the CO_2 induced corrosion less influenced by flow rate, due to its slow hydration process. Intensive research work has been done to investigate the relationship between corrosion rate and flow effect.

Morris, et al., reported that in the case of H_2S reduction at anode, with the increase of H_2S concentration at metal surface, the limiting current density was observed to gradually decrease to zero, which indicated H_2S reduction is charge transfer controlled [26].

Facilitating corrosion rate in cathodic reaction by increasing the flow velocity has also been experimentally verified by Galvan-Martinez's research group, where a rotating cylinder electrode was utilized for electrochemical test in pure H_2S solution under different rotation rate [27]. It is also indicated by the research work of Sun, et al., that corrosion rate can be drastically increased by accelerating flow rate [28]. Corrosion rate was found to increase from 0.45 mm/yr to 2 mm/yr with an increase in velocity from 0.5 m/s to 5 m/s at 25 °C, pH_2S 13.8 bar, and pCO_2 3.4 bar.

So in general, the higher flow rate is operated, the higher corrosion rate is expected, which has been verified by the comparison between the cases of corrosion with and without the formation protective scales [7, 21]. However, in many practical engineering applications, however, the flow conditions are more complicated, since there are more factors involved that impact the flow features, such as the separated flow zones due geometries of pipe (e.g., elbow, T-joints and U-bend) and secondary flow velocity in radial directions.

On the other hand, when there exists a protective scale on the metal surface formed from corrosion products, the effect of flow rate on corrosion rate is not obvious [5], which indicates the mass transfer rate is largely determined by the diffusivity of protective scales.

According to the investigation of using a rotating cylinder electrode by Sun, et al., the rotation rate plays an important role in impacting the initial corrosion rate of on bare metal surface, while the corrosion rate after 24 hours of exposure to the corrosive solution

is insensitive the change of rotating rate [28]. However, the study conducted in a flow loop by Omar, et al., indicated no obvious effects of flow on H_2S corrosion [29]. More interesting results were found in the review by Bonis, et al., where from over 100 reviewed different cases of sour field, low flow rates were found to result in severe corrosion, which is opposite to laboratory observations [30].

In addition, the formation of a protective scale from corrosion products is also under the impact flow, because the precipitation rate of iron sulfide (or iron carbonate) is determined by the concentrations of sulfide (or carbonate) ions at metal surface, which are affected by flow conditions. For the formation of iron sulfide, it is difficult to precipitate under the high flow velocity condition.

Another potential impact of the flow condition on corrosion is that wall shear stress at high flow rate is indicated to be able to mechanically damage the protective scales and initiate localized corrosion. For example, In the case H_2S corrosion with high flow velocities, it is likely that the formed and existed iron sulfide scales can be easily peeled off by the high rate flow, which then led the increase in corrosion rate. However, A substantial amount of research work has been done to investigate this impact [31], yet no significant effect of flow on mechanical damage on scales was discovered.

2.3.4 Mechanistic models

Mechanistic models are based on physical transport phenomena coupled with kinetics of chemical reactions, which are first principle mathematical derivations, to

describe the corrosion process. Although the models don't fully rely on the empirical correlations, but corrections are needed to make the models fit corrosion rates from experimental measurements.

One of the first mechanistic models for CO_2 corrosion was developed by Turgoose et al., in 1990s [32]. In their model, due to the existence of Nernst diffusion layer, which leads to the difference in concentrations between metal surface and bulk solution, an electrochemical model and a diffusion model were coupled together, and the approach on how to solve the involved equations were also demonstrated. Since the environment that the model simulated was a rotating disk electrode, the electrochemical model did not follow the standard Volmer-Butler mechanism. Instead, a hydrodynamic equation was applied to estimate the current density at the metal surface by simply coupling current density with the Nernst diffusion layer thickness together by using the relationship between the diffusion coefficients and the rotation frequency.

Fick's law was applicable for this case, and a hyperbolic PDE can be used to express all the mathematical problems in the model. Since it was a non-steady sate process expressed by PDE, numerical method by discretizing time steps and diffusion length was utilized. As shown in Figure 3, the boundary conditions are constant concentrations at the metal surface and in the bulk solution.

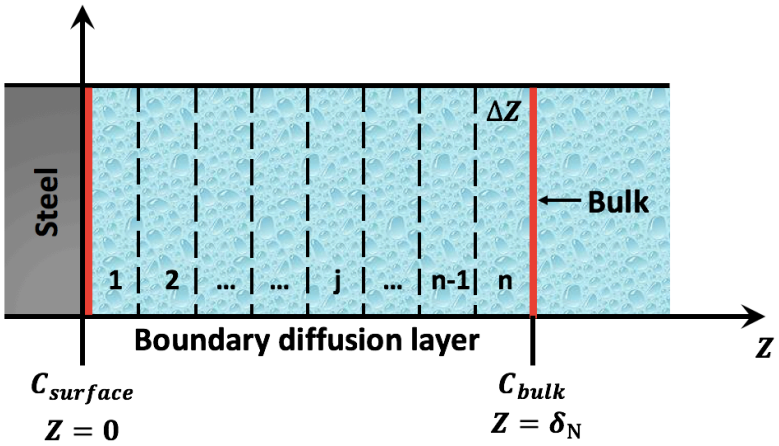

Figure 3. Corrosion diffusion model by Turgoose. Red lines are two boundaries at steel surface and bulk solution. The thickness of boundary diffusion layer is δ_N [32].

In this model, mass balance has been set up for every discretized length, by rewriting Equation (39) for specie i in space j in absence of chemical reaction ($R_i = 0$):

$$\left(\frac{dC_i}{dt}\right)_j = D_i \left(\frac{d^2C_i}{dz^2}\right)_j \tag{43}$$

To obtain the solution to specie concentrations on metal surface, we need solve this set of n coupled PDEs, which is difficult to be solved analytically. So slight change needs to make on the right side of equation by second order Taylor expansion:

$$\left(\frac{\partial^2 C_i}{\partial z^2}\right)_j = \frac{C_{j-1}+2C_j+C_{j+1}}{(\Delta z)^2} \tag{44}$$

Substituting Equation (44) back into Equation (43), we can obtain Equation (45). So the PDEs are converted into a set of coupled ordinary differential equations (ODEs), which make this model solvable numerically.

$$(dC_i)_j = \frac{D_i dt}{(\Delta z)^2}\left(C_{j-1} + 2C_{j+C_{j+1}}\right) \tag{45}$$

For next time step k+1, the calculation of concentration can be conducted by assuming $dC_i \approx \Delta C_i$, so the concentrations at time step k and k+1 can be linked by $(C_i)_{k+1} \approx (C_i)_k + (\Delta C_i)_k$.

On the right side of Nernst diffusion layer, the boundary condition is the bulk concentrations of corrosive species, which are assumed constant overtime, while the boundary condition on at metal surface follows the Faraday's Law for t > 0. Assuming the flux from diffusion layer to metal surface is equal to the flux of producing (or consuming) current at metal surface, it can be indicated that the concentration of species at metal surface also remains constant instead of being accumulated. The flux is expressed by current density in Faraday's law:

$$N_i = \pm \frac{v_i}{n_i F} i_i \tag{46}$$

where n is the number of electron exchanged for one mol specie i carry and v is the stoichiometric coefficients of species i in electrochemical reaction. For species that are consumed by electrochemical reaction, use positive sign; And negative sign is used for species generated by electrochemical reaction. For non-reacting or non-charged species, the flux is considered to be zero. Some examples of fluxes at metal surface are given by:

$$N_{Fe^{2+}} = -\frac{i_{Fe^{2+}}}{2F} \tag{47}$$

$$N_{H^+} = \frac{i_{H^+}}{F} \tag{48}$$

$$N_{H_2O} = 0 \tag{49}$$

The flux of Fe^{2+} is negative sign since Fe^{2+} is produced from the electrochemical reaction, while positive sign is applied for H^+ due to the consumption of hydrogen ion. The flux of water is zero because it is both non-charged and non-reaction specie. Although what the diffusion model can evaluate is the concentration profile of corrosive species at metal surface, once the concentration profile is coupled into electrochemical model, the corrosion rate can be obtained.

Figure 4 demonstrates the corrosion model by Sundaram et al., in 1996 [33], which constructed a comprehensive description on corrosion behavior.

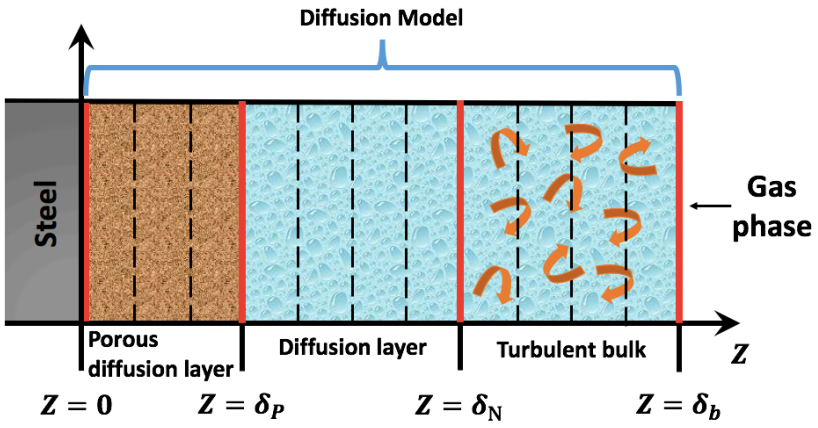

Figure 4. Corrosion model by Sundaram with three diffusion layers [33].

One major difference of this model from Turgoose's model is that the electrochemical kinetic model at the surface is incorporated. Another difference is the extension of diffusion model to three diffusion layers (porous diffusion layer, diffusion layer and turbulent bulk layer) from one in the Turgoose's model shown in in Figure 3. Considering the phase transition between the gas phase and the turbulent bulk layer, a mass transfer correlation was applied. Also, activities of species were coefficients were introduced so as to deal with equilibrium between the gas-liquid phase transition. Slightly different from Turgoose's diffusion model, the mass transport in diffusion layer was more detailed described with Nernst-Planck equation instead of Fick's Law, while the porous diffusion layer can fit Fick's Law and the diffusion in this layer was diffusion controlled. As a result, the concentration of transported species at metal surface ($z = 0$) is expected to be much lower than the concentration at the interface of porous layer and diffusion layer ($z = \delta_p$). The mass balance can be solved in steady state by using Equation (39), where $dC_i/dt = 0$, while $R_i \neq 0$. The existing problem of this model includes some missing parameters introduced in the model and reproducibility of the model.

As shown in Figure 5, the model developed by Dayalan et al., also includes a porous diffusion layer [34].

Similar to Sundaram's model, a mass transfer correlation was applied for mass transport, while for the mass transport in the porous diffusion layer, an effective diffusion coefficient D_{eff} was introduced to simplify the complexity of transport process. D_{eff} is proportional to the free diffusion coefficient (D) and the porosity of scales (ϕ) while

disproportional to the square of tortuosity (τ). Thus, the expression for effective diffusion coefficient is given by Equation (50):

$$D_{eff} = \frac{D\phi}{\tau^2} \tag{50}$$

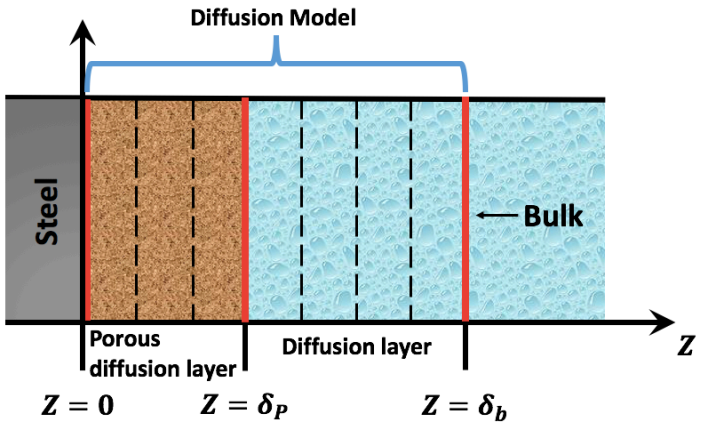

Figure 5. Corrosion model by Dayalan with two diffusion layers [34].

In the early of 2000s, Nesic et al., developed the Kjeller Sweet Corrosion (KSC) model, which is a more comprehensive corrosion prediction model [5, 6, 35, 36], which, as shown in Figure 6, is similar to the work done by Sundaram et al., and Dayalan et al.

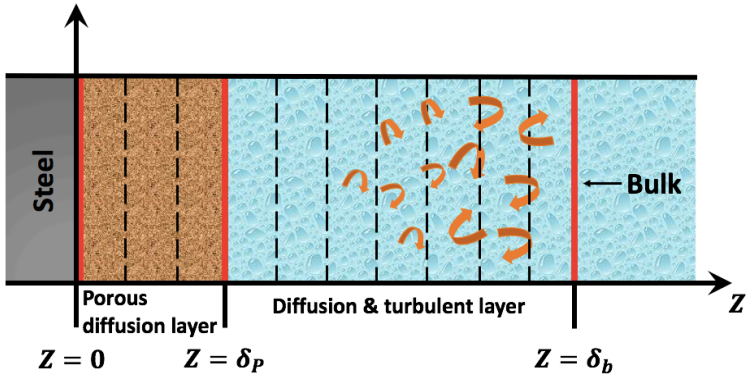

Figure 6. Corrosion model by Nesic with two diffusion layers and the diffusion coefficients are position dependent [35].

Throughout the diffusion & turbulent layer from bulk solution to metal surface, the concentration profile of corrosive species is dealt with Nernst-Planck equation, where the mass conservation is comparable to Equation (39) with the exception that some empirical corrections are applied to adjust the porosity of protective scale,

$$\frac{d(\varepsilon C_i)}{dt} = -\frac{d\left(\varepsilon^{1.5} N_i\right)}{dz} + \varepsilon \cdot R_i \tag{51}$$

where ε was the porosity of scale layer. Same with Turgoose's model, on the right side of Nernst diffusion layer, the boundary condition is the bulk concentrations of corrosive species, which are assumed constant overtime, while the boundary condition on at metal surface follows the Faraday's Law for t > 0. The KSC model was able to calculate corrosion rate, since the diffusion model discussed above was coupled with an electrochemical model by utilizing Equation (46). The diffusion coefficients are different depending on the layers of mass transport due to the induced factors such as tortuosity in porous layer and turbulence in turbulent diffusion layer. Thus, ε and D_i (free diffusion

coeffiecient) changes as the location in the diffusion layers changes. It was estimated by Nesic et al., that ε ranges from 0.1 to 0.6 when z moves from zero to δ_P. For the mass transport from $z = \delta_P$ to $z = \delta_b$, $\varepsilon = 0.6$ was assumed. In addition, an effective diffusion coefficient (D_{eff}) was applied by summing the total effect of free diffusion (D_i) and turbulence contribution to diffusion (D_t).

$$D_{eff} = D_i + D_t \tag{52}$$

where, for $\delta_P < z < \delta_b$,

$$D_t = 0.18\left(\frac{x-\delta_P}{\delta_b-\delta_P}\right)^3 \frac{\mu}{\rho} \tag{53}$$

Here, $(\delta_b - \delta_P)$ represents the thickness of diffusion & turbulence layer, which is can be correlated with Reynold's number by Equation (54):

$$(\delta_b - \delta_P) = 25Re^{-7/8}d \tag{54}$$

where d is the hydraulic diameter and $Re = \rho v d/\mu$, v is velocity of bulk flow, ρ and μ are density and viscosity of the bulk solution, respectively.

Recently, Zhang and Nesic et al., developed an advanced H_2S/CO_2 mechanistic model based on the principles FREECORP and MULTICORP corrosion models [37]. The set-up of the model is pretty much similar with KSC, as shown in Figure 7.

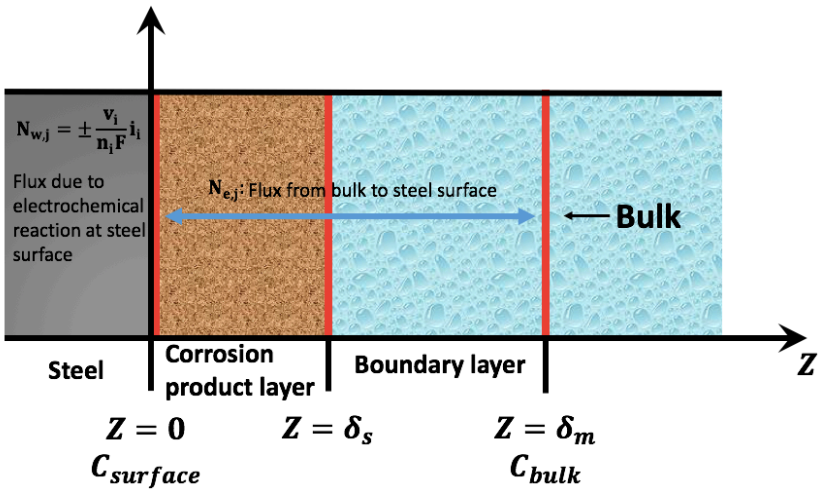

Figure 7. Corrosion model by Zhang and Nesic et al., with two diffusion layers which are treated as a single mass transport domain [37].

Different from the approach in KSC model dealing with the mass transport in different types of diffusion layer, concentration profile of species is not calculated throughout the mass transfer boundary layer, due the complexity and long computation time involved in KSC model. Instead, only two nodes are considered, one is the concentration of species in the bulk, which can be easily obtained from water chemistry model mentioned section 2.2, the other is the concentration at steel surface, which can be calculated with mass transfer flux by using a mass transfer coefficient, $k_{T,j}$, which is related with flow conditions of bulk solution, as well as the tortuosity and the porosity of product layer. The mass transport of this corrosion model is described by Equation (55), which is pretty much similar with Nernst-Planck Equation:

$$\Delta z \frac{\partial \varepsilon C_{surface,j}}{\partial t} = \pm \frac{i_j}{n_j F} + k_{T,j}\left(C_{bulk,j} - C_{surface,j}\right) + \frac{z_j F}{RT} C_{bulk,j} \Delta \Phi + \Delta z \cdot R_j \quad (55)$$

where, $k_{T,j}$ is the function of $k_{s,j}$ and $k_{m,j}$. $k_{m,j}$ is the mas transfer coefficient in boundary layer and $k_{s,j}$ is the mas transfer coefficient in corrosion product layer

$$\frac{1}{k_{T,j}} = \frac{1}{k_{s,j}} + \frac{1}{k_{m,j}} \tag{56}$$

The model was able to predict the H_2S/CO_2 corrosion rate by estimating: water chemistry in the bulk solution and steel surface, electrochemical kinetics at the steel surface, as well as the formation of corrosion product and growth of protective scales. The one of the keys of this model to incorporate different factors together is the mass transfer coefficient, and it is significantly impacted by flow velocity of bulk solution. However, this model does not consider the effect of flow conditions on the velocity distribution in the whole pipe as well as the effect on the damage of protection scale.

Recently, there have been some research works carried out to develop a flow field model in a pipe and then couple with a corrosion model to simulate the flow assited corrosion (FAC) [38-40].

Das and coworkers conducted a comparative investigation in different turbulence models in simulating the flow-assisted corrosion (FAC) process for pipes with noncircular cross sections and bends [41]. As shown in Figure 8, due to the special geometry of U-bend pipe, the flow velocities at different locations were analyzed. And the corrosion rate at corresponding locations were also estimated by coupling the results from the flow field model into the corrosion model.

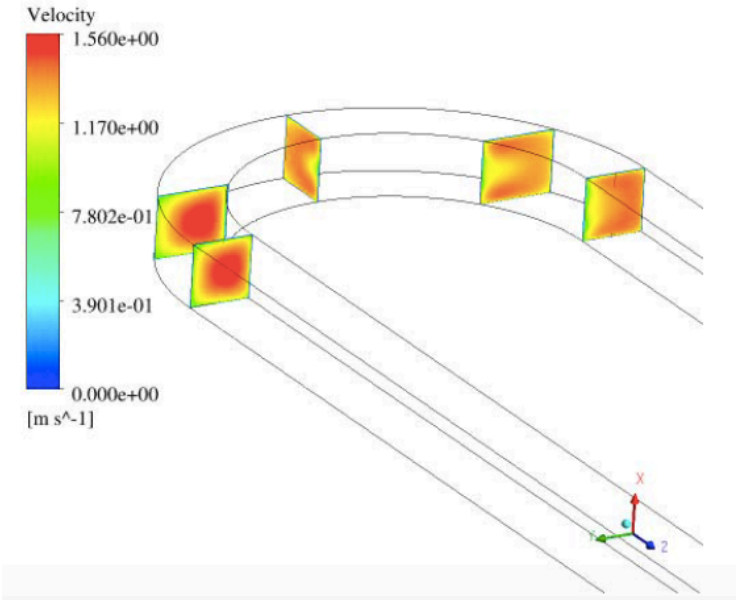

Figure 8. Velocity distribution at cross sectional planes within the bend section of a pipe [41].

In another paper published by Cui et al., in 2014, a H_2S/CO_2 corrosion model was developed to predict the uniform corrosion rate in pipe [42]. In this model, the flow parameters were simulated by CFD based on turbulence theory including flow velocity, turbulent kinetic energy and phase distribution. Then the flow condition model was coupled with the corrosion model to generate a "map: of corrosion rate, as shown in this Figure 9, at different locations in the pipe.

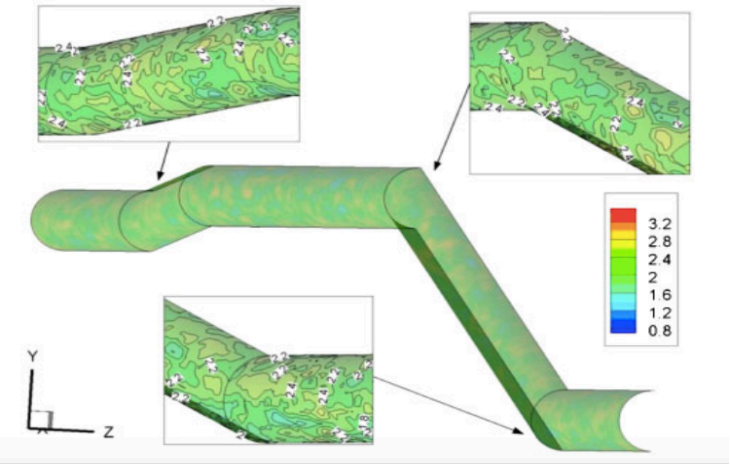

Figure 9. Contour map of corrosion rate calculated the model of by Cui et al., in a pipe [42].

However, the corrosion model used in this paper is an empirical model, which does not have comprehensive description in mass transport of corrosive species, electrochemical reactions on steel surface and the formation of protective scales.

CHAPTER III

METHODOLOGY AND MODEL DEVELOPMENT

In most engineering practice, the flow condition within a pipe is always turbulent. In addition, corrosion process involves mass transport to transfer the corrosive species to steel surface for electrochemical reaction. Furthermore, all pipes include elbows with the associated complex flow features, which makes the model more complicated. Based on the literature review in Chapter 2, most of the published mechanistic model on corrosion prediction in pipes focused on either a single straight pipe with an one-dimensional mass transport model, which were not applicable to describe the complex mass transport process in a elbow under turbulent condition, which is important for the prediction of corrosion rate distribution in an elbow or band of pipe.

Since the flow condition determines the mass transport coefficient, while mass transport coefficient determines the concentrations of corrosive species at steel surface, which is proportional to the corrosion rate, a better description on the flow condition and mass transport in an elbow is very helpful for predicting corrosion rate. Due to the strong influence of local mass transfer coefficients on corrosion rate predictions, prediction models for corrosion in a bend or a 90° elbow have been developed to correlate mass transport coefficient with corrosion rate [40, 41, 43, 44]. However, all these models calculated the mass transfer coefficient with a numerical method, where the concentrations of corrosive species were assumed to be zero, then directly correlated the mass transfer coefficient to corrosion rate. In this case, the corrosion rate is solely mass-transfer

controlled, and it is difficult to incorporate electrochemical reaction and scale formation into the model.

In the present study of this thesis, an electrochemistry model is constructed to describe the electrochemical reaction and corrosion rate at steel surface. Also, a mass transport model containing mass transport and water chemistry in both boundary layer and bulk layers is developed, which is then incorporated into the electrochemistry model. Then the flow model in an elbow is developed to obtain the information such as surface shear stress, boundary layer thickness and turbulent diffusivity. At last, the flow model is linked together with other two models by the transferable data.

3.1 Electrochemistry model

3.1.1 Cathodic reaction

H^+ reduction

Hydrogen ions dissociated from either H_2S or H_2CO_3 are most readily reduced specie due to its large diffusion coefficient compared to other species. As expressed in Equation (55), The total current density from the reduction of H^+ includes two parts: the charge transfer current density and diffusion limit current density,

$$\frac{1}{i_{H^+}} = \frac{1}{i_{\alpha,H^+}} + \frac{1}{i^d_{lim,H^+}} \tag{57}$$

where, i_{H^+} is the total current density of H^+ reduction, i_{α,H^+} is the charge transfer current density and i^d_{lim,H^+} is the diffusion limit current density. For the charge transfer current density, it can be expressed as Equation (58):

$$i_{\alpha,H^+} = i_{0,H^+} \times 10^{-\frac{\eta}{\beta_c}} \tag{58}$$

where, β_c is the Tafel slope as mentioned in Chapter 2. According to Bockris [45], for H^+ reduction, β_c is 120 mV/decade at 30 °C when α_c= 0.5. And this number is consistent with the experimental result of Zheng, et al. F is Faraday constant (F = 96,485.33 s·A/mol)

$$\beta_c = \frac{2.303RT}{\alpha_c F} \tag{59}$$

η is the difference between the applied potential E and reversible potential E_{rev} (or corrosion potential E_{corr}), and the reversible potential of hydrogen ion reduction is related with the pH value of solution. Due to extremely low partial pressure of H_2, the second term in Equation (60) can be ignored during calculation.

$$E_{rev(H^+)} = -\frac{2.303RT}{F}\mathrm{p}H - \frac{2.303RT}{2F} log P_{H_2} \tag{60}$$

The calculation of exchange current density (i_{0,H^+}) is shown in Equation (61), where the reference exchange current density (i_0^{ref}) is chosen to be 0.03 A/m^2 at the reference temperature (T_{ref} = 298.15 K) and the reference concentration of hydrogen ion (C_{H^+ref} = 10^{-4} M). 30 kJ/mol is taken for the enthalpy of activation as indicated by Nordsveen, et al., in 2003[6].

$$i_{0,H^+} = i_0^{ref}\left(\frac{C_{H^+\_S}}{C_{H^+ref}}\right)^{0.5} \times e^{-\frac{\Delta H}{R}\left(\frac{1}{T}-\frac{1}{T_{ref}}\right)} \quad (61)$$

For diffusion limit current density, it can be calculated by Equation (62). k_{m,H^+} is mass transport coefficient of hydrogen ion (m/s), which can be determined from the flow condition model discussed in the later section of this chapter. And $C_{H^+}$is the concentration in bulk.

$$i_{lim,H^+}^d = k_{m,H^+} F C_{H^+\_b} \quad (62)$$

So the unknowns for calculation charge transfer current density are the applied potential (E) and H^+ concentration at steel surface ($C_{H^+\_S}$), and the later can be solved from the mass transport model in the later section of Chapter 3.

H_2S reduction

Besides the reduction of hydrogen ions, the dissolved H_2S can also be reduced to contribute to corrosion process. The total current density of H_2S reduction is also consist of charge transfer current density and diffusion limit current density, which is given by Equation (63):

$$\frac{1}{i_{H_2S}} = \frac{1}{i_{\alpha,H_2S}} + \frac{1}{i_{lim,H_2S}^d} \quad (63)$$

For the calculation of charge transfer current density, β_c= 120 mV was determined from experiments at 30 °C by Zheng, et al., [46], which same with hydrogen ion. And

$E_{rev(H_2S)}$ is calculated by Equation (65), where the partial pressure of H_2S (P_{H_2S}) is considered.

$$i_{\alpha,H_2S} = i_{0,H_2S} \times 10^{-\frac{\eta}{\beta_c}} \tag{64}$$

$$E_{rev(H_2S)} = -\frac{2.303RT}{F} pH - \frac{2.303RT}{2F} logP_{H_2S} \tag{65}$$

For the calculation of exchange current, i_0^{ref}=0.00015 A/m^2 at T_{ref} = 293.15 K, C_{H_2Sref} = 10^{-4} M and C_{H^+ref} = 10^{-4} M, The enthalpy of activation is taken to be 60 kJ/mol, which was in good agreement of experiment results[46].

$$i_{0,H_2S} = i_0^{ref} \left(\frac{C_{H_2S\_S}}{C_{H_2Sref}}\right)^{0.5} \left(\frac{C_{H^+\_S}}{C_{H^+ref}}\right)^{-0.5} \times e^{-\frac{\Delta H}{R}\left(\frac{1}{T}-\frac{1}{T_{ref}}\right)} \tag{66}$$

Similar with the calculation in Equation (62), the diffusion limit current density of H_2S is expressed in Equation (67), where the mass transport coefficient is solved from flow condition model as well, and the bulk concentration of H_2S is solved from Equation (29) and (34) by given the partial pressure of H_2S.

$$i_{lim,H_2S}^d = k_{m,H_2S} F C_{H_2S\_b} \tag{67}$$

H_2CO_3 reduction

Similar with H_2S, H_2CO_3 formed from the dissolved CO_2 can also be directly reduced by electrochemical reaction at steel surface. As shown in Equation (68), the total

current density is consisting of charge transfer current density and hydration limit current density.

$$\frac{1}{i_{H_2CO_3}} = \frac{1}{i_{\alpha,H_2CO_3}} + \frac{1}{i^r_{lim,H_2CO_3}} \tag{68}$$

$$i_{\alpha,H_2CO_3} = i_{0,H_2CO_3} \times 10^{-\frac{\eta}{\beta_c}} \tag{69}$$

$$\beta_c = \frac{2.303RT}{\alpha_c F} \tag{70}$$

For charge transfer current density of H_2CO_3 reduction, , β_c is approximate to 120 mV/decade, when α_c is equal to 0.5 at 30 °C. Similar with H_2S, the reversible potential of H_2CO_3 reduction is a function of CO_2 partial pressure (see Equation (71)).

$$E_{rev(H_2S)} = -\frac{2.303RT}{F} pH - \frac{2.303RT}{2F} logP_{CO_2} \tag{71}$$

For the calculation of exchange current, i_0^{ref}=0.018 A/m^2 at T_{ref} = 293.15 K, $C_{H_2CO_3 ref}$ = 10^{-4} M and $C_{H^+ ref}$ = 10^{-4} M, The enthalpy of activation is taken to be 50 kJ/mol [4, 6].

$$i_{0,H_2CO_3} = i_0^{ref} \left(\frac{C_{H_2CO_3\_S}}{C_{H_2CO_3 ref}}\right)^{0.5} \left(\frac{C_{H^+\_S}}{C_{H^+ ref}}\right)^{-0.5} \times e^{-\frac{\Delta H}{R}\left(\frac{1}{T}-\frac{1}{T_{ref}}\right)} \tag{72}$$

The hydration limit current density is calculated by Equation (73) [4],

$$i^r_{lim,H_2CO_3} = f \times F \times C_{CO_2\_b} \times \left(D_{H_2CO_3} K_{hyd} k^f_{hyd}\right)^{0.5} \tag{73}$$

where K_{hyd} is the CO_2 hydration constant equal to 0.00258 and the k_{hyd}^{f} is the forward hydration reaction constant which is calculated in Equation (74) [2015 Zheng: 25]:

$$k_{hyd}^{f} = 10^{329.85-110.541\times logT_k-\frac{17265.4}{T_k}} \tag{74}$$

The concentration of dissolved CO_2 in bulk $C_{CO_{2\_b}}$ is calculated by Equation (12) and (21).

H_2O reduction

Since the corrosion model in this thesis considers single-phase condition with H_2O as solvent, the total current density of H_2O reduction is purely equal to its charge transfer current density. Therefore:

$$i_{H_2O} = i_{\alpha,H_2O} = i_{0,H_2O} \times 10^{-\frac{\eta}{\beta_c}} \tag{75}$$

where, β_c is equal to 120 mV/decade at 30 °C or can be calculated by Equation (59) [47]. Since the thermodynamics of reduction of H_2O and H^+ are similar, the reversible potential of H_2O can also be calculated by Equation (60) [46].

According to Zheng, et al., for the calculation of exchange current density for H_2O in the presence of H_2S (Equation (69)), the reference exchange current density (i_0^{ref}) and the enthalpy of activation are taken to be 10^{-6} A/m^2 and 90 kJ/mol, respectively, while the C_{H_2Sref} and C_{H^+ref} are same with the value taken for H_2S reduction.

$$i_{0,H_2O} = i_0^{ref}\left(\frac{C_{H_2S}}{C_{H_2Sref}}\right)^{-0.1}\left(\frac{C_{H^+}}{C_{H^+ref}}\right)^{-0.5} \times e^{-\frac{\Delta H}{R}\left(\frac{1}{T}-\frac{1}{T_{ref}}\right)} \quad (76)$$

HS^- and HCO_3^- reduction

Since both HS^- and HCO_3^- are negatively charged, the reduction of two species are more thermodynamically difficult than H^+, H_2S, H_2CO_3 and H_2O. Thus, the reduction of than H^+, H_2S, H_2CO_3 and H_2O are dominant in corrosion process, while the reduction of HS^- and HCO_3^- can be ignored.

3.1.2 Anodic reaction

Fe oxidation with OH^-

Current density at anode due to the oxidation of iron is expressed in Equation (77), which is only related with charge-transfer current density, since the diffusion process involved in the iron dissolution can be ignore as compared with the diffusion of other species.

$$i_{Fe} = i_{0,Fe} \times 10^{\frac{\eta}{\beta_a}} \quad (77)$$

The Tafel slope for iron oxidation ranges from 40 mV/decade to 50 mV/decade with or without the presence of H_2S.

$$\beta_a = \frac{2.303RT}{\alpha_a F} \quad (78)$$

According to Bockris, et al., β_a is 38.9 mV/decade, when the apparent symmetry coefficient for the anodic reaction of Fe dissolution was taken as 1.5 at 30 °C [45]. This value is in good agreement with Zheng's experimental results [46, 48]. The reversible potential of Fe was -0.488 V for X65 steel [4].

The exchange current density is as expressed in Equation (23). The exchange current density is proportional to the adsorption of OH^- ions (θ_{OH^-}) on steel surface, which is correlated with the concentration of OH^- ions at steel surface by Frumkin adsorption model (Equation (80)) [48].

$$i_{0,Fe} = i^*_{0,Fe}\theta_{OH^-}e^{-\frac{\Delta H}{R}\left(\frac{1}{T}-\frac{1}{T_{ref}}\right)} \quad (79)$$

$$K_1 C_{OH^-} = \frac{\theta_{OH^-}}{1-\theta_{OH^-}}e^{(-f\theta_{OH^-})} \quad (80)$$

According to Bockris, et al., the best-fit values for Equation (79) and (80) are $i^*_{0,Fe}$= 0.25, K_1= 1.56×10^9, f = 3.83, ΔH=37.5 kJ/mol and T_{ref} = 293.15 K [45]. The concentration of OH^- ion can be calculated by Equation (20) and (25)

Fe oxidation with HS^-

When in the acidic solution with the presence of H_2S, the concentration of OH^- ions at steel surface is much lower than HS^-, even with a small amount of H_2S in the gas phase (e.g., 100 ppm). Thus, the anodic adsorption is dominated by HS^-, while the effect of OH^- can be ignored. The expressions of exchange current density for anodic reaction

controlled by HS^- concentration Equation (81) and (82) are similar to the of exchange current density controlled by OH^- concentration.

$$i_{0,Fe} = i_{0,Fe}^{*\prime}\theta_{HS^-}e^{-\frac{\Delta H}{R}\left(\frac{1}{T}-\frac{1}{T_{ref}}\right)} \tag{81}$$

$$\theta_{HS^-} = \frac{K_2 C_{HS^-}}{1+K_2 C_{HS^-}} \tag{82}$$

According to Zheng and Nesic [46, 48], the best-fit values in Equations (81) and (82) are $i_{0,Fe}^{*\prime}$ = 0.33, $K_2 = 3.5\times10^6$, , ΔH=37.5 kJ/mol and T_{ref} = 293.15 K. The concentration of HS^- ion can be calculated by Equation (31) and (35).

3.1.3 The mixed potential theory

As mentioned in the derivation of corrosion rate in Equation (10) in Chapter 1, the corrosion rate is proportional to the either cathodic current density or anodic current density. In order to calculate the current densities, the steel surface concentrations can be obtained from the mass transport model in the later section, while the applied potential (E) can be calculated by using the mixed potential theory and solving the charge balance equation (Equation (83) and (84)). Since total cathodic current density and total the anodic current density are with opposite signs, and the total current density at steel surface is zero.

$$\sum i_{anodic} = \sum i_{cathodic} \tag{83}$$

$$i_{Fe} = i_{H^+} + i_{H_2S} + i_{H_2O} + i_{H_2CO_3} \tag{84}$$

Once the applied potential is solved by Equations (84), the corrosion rate can be immediately determined.

3.2 Mass transport model

According to the description on the electrochemistry model, corrosive species such as H^+, H_2S and H_2CO_3 are consumed at steel surface while Fe^{2+} are generated, which resulted in the concentration gradients that trigger the molecular diffusions with corrosive species being diffused to the steel surface while Fe^{2+} ions being diffused away. Since the rate of electrochemical reactions at steel surface is much faster than the diffusion process, the concentrations of corrosive species are so different from the bulk concentrations, which means that using bulk concentrations for the calculation of corrosion current density and rate will lead to inaccuracy. Instead, the corrosion rate is more dependent on the concentrations at steel surface. Therefore, the surface concentration of different corrosive species is the key to couple the electrochemical reactions and the mass transport in the boundary layer.

Normally, since different corrosive species have different diffusion coefficients, as listed in Table 6, and the equilibrium chemical reactions that dissociate positively and negatively charged ions are accompanied with the diffusion process, the charges will be separated due to the difference in diffusion coefficients, which then leads to the generation of potential gradient and electro-migration of charged species. However, due to the fact

that the aqueous solution with corrosive species in the current model is so diluted, the contribution of electro-migration to mass transport can ignored in this case.

Table 6. Diffusion coefficient of corrosive species involved in current model

Species	Diffusion coefficient (m^2/s)	Source
H^+	9.312×10^{-9}	[49]
OH^-	5.26×10^{-9}	[49]
H_2S	1.61×10^{-9}	[50]
HS^-	2.00×10^{-9}	[6]
S^{2-}	2.00×10^{-9}	[6]
CO_2	1.96×10^{-9}	[50]
H_2CO_3	2.00×10^{-9}	[51]
HCO_3^-	1.105×10^{-9}	[49]
CO_3^{2-}	0.92×10^{-9}	[51]
Fe^{2+}	0.72×10^{-9}	[51]

The mass transport process for listed species is demonstrated in Figure 10. Here only one-dimensional mass transport along the radial direction is considered, which will be then coupled with three-dimensional flow model of pipe and elbow. Due to the complexity of corrosion product scale formation mechanism and the fact that the scale formation is dependent on the species concentration on bare steel surface, the diffusion barrier effect of protective scale is not taken into consideration in the current model, but the solution conditions on whether protective scales can form will be discussed in the later section.

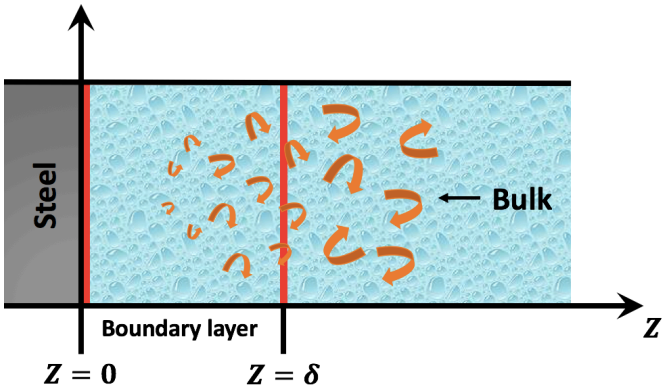

Figure 10. One-dimensional mass transport model for corrosives species transferred from bulk to steel surface

It is assumed that turbulent mixing is dominant in the bulk solution, so the species concentration in the bulk is considered to be constant. This assumption is also extended to apply for the flow model, so the concentration of different species throughout the pipe is treated as constant as well.

As for the mass transport in the boundary layer, mass conservation equation is applied to be the governing equation for all species, which is expressed in Equation (85).

$$\frac{\partial C_i}{\partial t} = -\frac{\partial N_i}{\partial z} + R_i \tag{85}$$

where C_i is the concentration of specie i, N_i is the flux of specie i and R_i is the equilibrium chemical reactions that specie i is involved in. Equilibrium chemical reactions R_i for the species listed in Table 6 has been elaborated in Chapter 2. The flux of species N_i can be expressed by Equation (86):

$$N_i = -D_i \frac{\partial c_i}{\partial z} - z_i u_i F c_i \frac{\partial \phi}{\partial z} + c_i u \tag{86}$$

The first term is on the right side of Equation (86) is the flux contributed by molecular diffusion. Again, as mentioned previously, due to the diluted solution, the migration due to charge separation can be ignored. The third term is mass transport due to the convection in radial direction. In the boundary layer of turbulent flow, it is complicated and time consuming to compute the instantaneous velocity (u) in the third term. According to Nesic et al., [6], the convection term arising from the presence of eddies can be approximately replaced by $-D_t \frac{\partial c_i}{\partial z}$, which is called turbulent diffusivity term [52]. So Equation (86) becomes:

$$N_i = -(D_i + D_t) \frac{\partial c_i}{\partial z} \tag{86}$$

where, D_t is called turbulent diffusion coefficient, which changes with distance from the steel surface and is a function of boundary layer thickness [52]:

$$D_t = 0.18 \left(\frac{z}{\delta}\right)^3 \frac{\mu}{\rho} \qquad (0 \le z \le \delta) \tag{87}$$

In order to obtain the concentration profile in the boundary layer, the boundary layer thickness at different points of steel surface in the pipe should be determined. According to Cengel [53], the thickness of boundary layer is approximated as a function of shear stress of pipe wall:

$$\delta = \frac{5v}{\sqrt{\tau_w/\rho}} \tag{87}$$

where v is the kinematic viscosity of solvent and τ_w is the shear stress at pipe wall, which can be obtained from the flow field model describe in the following section. If only considering the steady state mass transport process, Equation (85) becomes:

$$0 = (D_i + D_t)\left(\frac{\partial^2 C_i}{\partial z^2}\right) + R_i \tag{88}$$

Therefore, for ten species, there are ten of this ordinary differential equations, which are coupled by equilibrium chemical reactions (R_i). The boundary conditions for solving the OEDs are the constant concentration in bulk solution and total current density at steel surface being zero. Since the electrochemistry model and the mass transport model are coupled by the boundary condition, the concentration of corrosive species at steel surface and corresponding current density can be easily solved by the electrochemistry module incorporated in COMSOL software.

3.3 Flow model in pipe and elbow

In order to obtain the information of shear stress and boundary layer thickness as mentioned in the electrochemistry and mass transport model, a flow model is needed to calculate the shear stress distribution at pipe wall. In most engineering practice, flow condition within a pipe is almost turbulent, so $k - \omega$ model is chosen to simulate the single phase turbulent flow in the pipe and elbow.

Different from $k-\varepsilon$ model, $k-\omega$ solves the specific rate of dissipation of kinetic energy. One of the advantages of $k-\omega$ model is the near wall treatment, which is more accurate than $k-\varepsilon$ model to simulate internal flows with strong curvature such as flows in pipe bend and 90° elbow, and give better computation results of shear flow spreading.

As expressed by Equation (89) and 90°, the standard $k-\omega$ model is a two-equation model solving the turbulence kinetic energy (k) and the specific rate of dissipation (ω) (the rate that turbulence kinetic energy k converts into internal thermal energy):

$$\frac{\partial}{\partial t}(\rho k)+\frac{\partial}{\partial x_j}(\rho k u_j)=\frac{\partial}{\partial x_j}\left[\left(\mu+\frac{\mu_t}{\sigma_k}\right)\frac{\partial k}{\partial x_j}\right]+G_k-Y_k+S_k \tag{89}$$

$$\frac{\partial}{\partial t}(\rho \omega)+\frac{\partial}{\partial x_j}(\rho \omega u_j)=\frac{\partial}{\partial x_j}\left[\left(\mu+\frac{\mu_t}{\sigma_\omega}\right)\frac{\partial \omega}{\partial x_j}\right]+G_\omega-Y_\omega+\mathrm{S}_\omega \tag{90}$$

where,

$G_k=\rho\tau_{ij}\frac{\partial u_i}{\partial x_j}$, generation of turbulent kinetic energy due to mean velocity gradients;

$G_\omega=\alpha\frac{\omega}{k}\tau_{ij}\frac{\partial u_i}{\partial x_j}$, generation of specific rate of dissipation;

$Y_k=\beta^*\rho\omega k$, dissipation of k due to turbulence;

$Y_\omega=\beta\rho\omega^2$, dissipation of ω due to turbulence;

S_k and S_ω represents source terms;

$\mu_t = \frac{\rho k}{\omega}$;

$\alpha = \frac{5}{9}$;

$\beta^* = 0.09$;

$\beta = 0.075$;

$\sigma_k = \sigma_\omega = 2$;

Here in this this thesis, the model is to simulate the corrosion rate distribution in a 90 ^{o} elbow connecting two pieces of straight pipe in a refinery facility of Assiut Oil Refining Company (ASORC), with the exception that only single liquid phase flow (water) is considered. Then the results of the model are compared with the published results by Doheim *et al.*, [44]. The configuration of pipes and elbow is as shown in Figure 11, and the corresponding geometry and operation parameters are listed in Table 7.

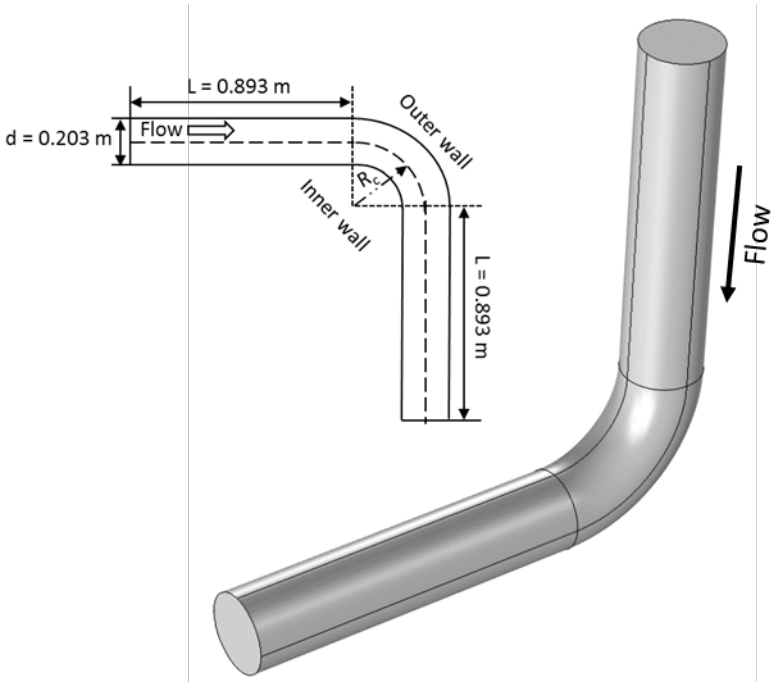

Figure 11. Configuration of pipe and 90° elbow of ASORC

Table 7. Geometry and operation parameters

d	0.203 [m]	Pipe diameter
L	0.893 [m]	Inlet and outlet pipe length
R_c	0.305 [m]	Radius of curvature
u	0.19 [m/s]	Average flow velocity
P	1.91 [bar]	Operating pressure
μ	0.000355 [kg/(m•s)]	Dynamic viscosity of water
ρ	971.8 [kg/m^3]	Density of water

In order to make sure that the flow in the inlet pipe on one side of elbow is fully developed, a two-dimensional axisymmetric model is constructed with the length of 100

diameters of pipe. The outlet results from the two-dimensional pipe are mapped onto the inlet boundary of the three-dimensional geometry by using coupling variables, which can be easily achieved in COMSOL.

The meshing of the geometry of pipe is completed in COMSOL, which is demonstrated in Figure 12. The mesh is constructed to approximately match what is used by Doheim *et al.*, [44], with the exception that the mesh in the bend itself is unstructured. In order to obtain the results with higher resolution in the boundary layer adjacent to the steel surface, more refined meshes are applied near the pipe wall, as shown in the cross-section enlarged in Figure 12. This is necessary for obtaining more accurate results of surface shear stress. Finally, the number of cells contained in the entire flow model from this meshing is 24,535.

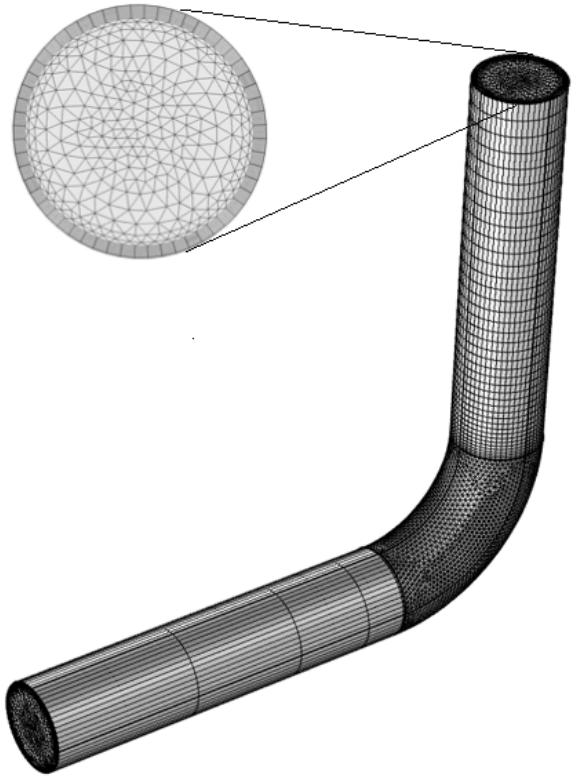

Figure 12. Mesh of pipe and 90° elbow

The results that needs to extracted from the flow model are the shear stress (τ_w) on steel surface and the mass transport coefficient (k_m), which is correlated with diffusion limit current density as mentioned in the previous section. According to the Liu *et al.,* and Rani *et al.,* [54, 55], mass transport coefficient is proportional to shear stress under the turbulent condition based on the Chilton-Colburn equation.

$$k_m = \left(\frac{\tau_w}{u\rho}\right) Sc^{-2/3} \tag{91}$$

where, u is average flow velocity and Sc is Schmidt number:

$$Sc = \frac{\mu}{\rho D_i} \tag{92}$$

CHAPTER IV

RESULTS AND DISCUSSION

4.1 Analysis of hydrodynamic parameters

The simulation results of two-dimensional flow model is as shown in Figure 13. The turbulent dynamic viscosity at the centerline maintains almost as a constant after distance of 60 pipe diameters while far before the outlet. This indicates that the flow has already been fully developed at the outlet, and it is appropriate to apply the outlet conditions to the three-dimensional flow model as the boundary conditions.

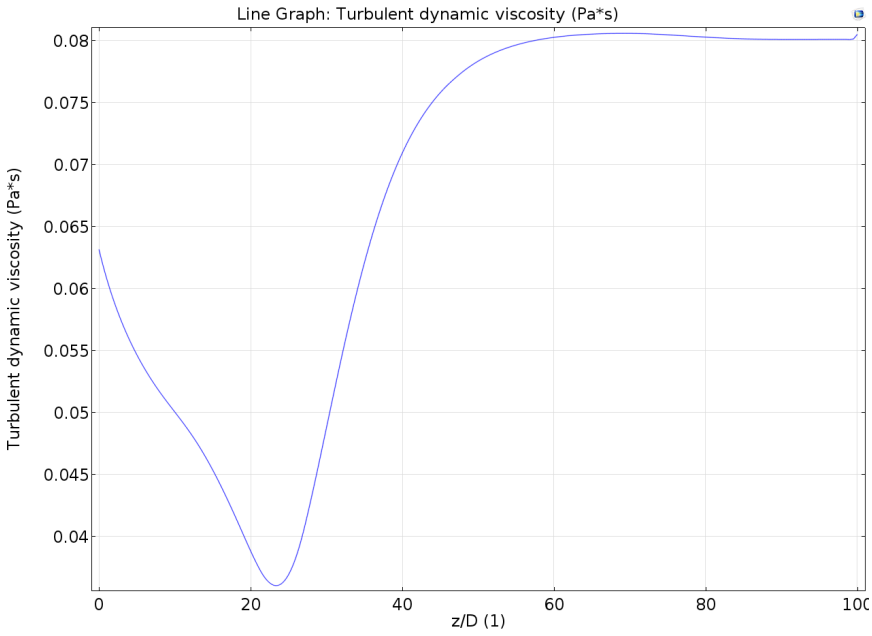

Figure 13. The change of turbulent dynamic viscosity as a function of position in the two-dimensional straight pipe

The distribution of the shear stress for the different separation distances (upstream, elbow and downstream) are shown in Figure 14. The distribution shows almost uniform and identical shear stress in the upstream pipe. The wall shear stress distribution starts to be diversified at the inlet of 90^{o} elbow and throughout the elbow in the downstream direction, with the sharp increase in the inner wall and drastic decrease in the outer wall. As the flow go through the elbow, the shear stress increases at the outer wall near exit, while static zone is observed at the inner wall near exit. This adverse separation in the wall shear stress distribution continues into downstream pipe.

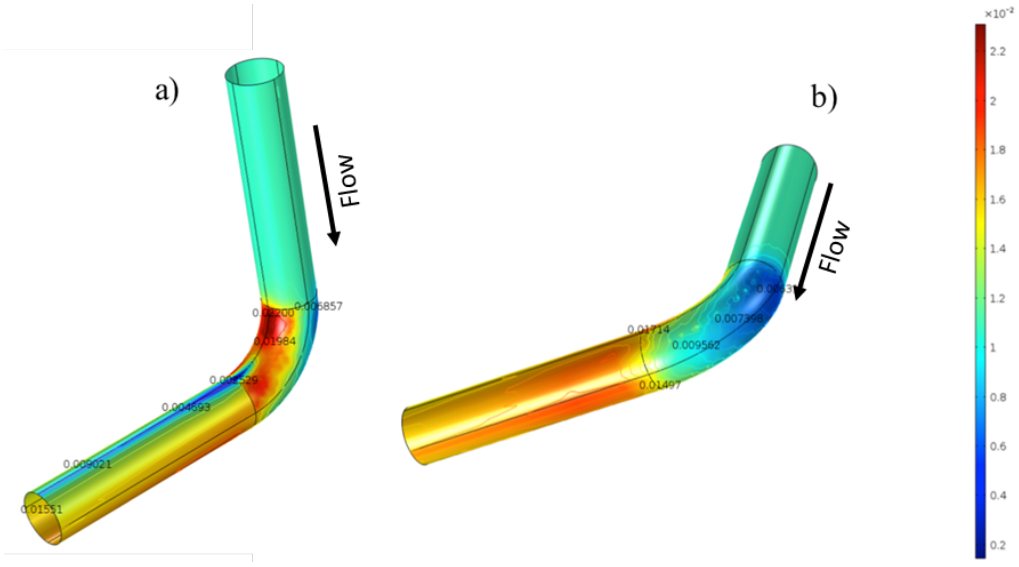

Figure 14. Shear stress (τ_w [Pa]) distribution in the pipe and 90^{o} elbow with the view on a) inner wall and b) outer wall

As mentioned by the correlation of $k_m = \left(\frac{\tau_w}{u\rho}\right) Sc^{-2/3}$ in Chapter 3 that mass transfer coefficient is proportional to wall shear stress. As can be observed in Figure 15, the distribution of mass transfer coefficient of H^+ follows the same pattern of wall shear stress distribution, which is in a good agreement with Liu *et al.,* and Rani *et al.,* [54, 55].

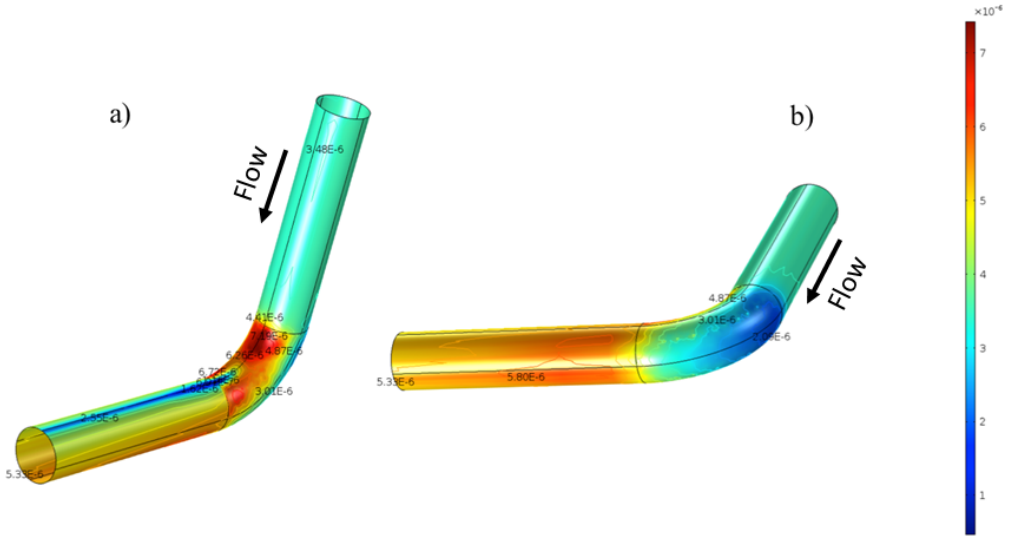

Figure 15. Mass transfer coefficient (k_m [m/s]) distribution of H^+ in the pipe and 90° elbow with the view on a) inner wall and b) outer wall

In general, the increase in both wall shear stress and mass transfer coefficient in a flow regime would increase corrosion rate at the steel. The increase in wall shear stress will result in the decrease in thickness of boundary layer (see Figure 16), according to Equation (87). As a result, the mass transport from bulk to steel surface will be facilitated,

which can increase the corrosion rate by increasing the diffusion limit current density and the concentration of corrosive species at steel surface.

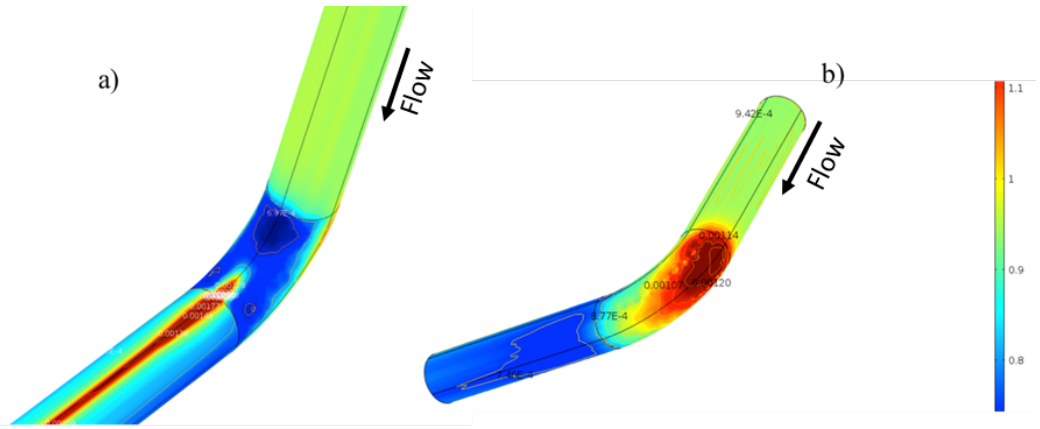

Figure 16. Boundary layer thickness (δ [m]) distribution in the pipe and 90^o elbow with the view on a) inner wall and b) outer wall

As shown in Figure 17, the pressure contours in the pipe and elbow, the pressure increases at outer wall as the flow moves from inlet of elbow to about 45^o position, while the pressure along the inner wall decreases to negative values. This indicates that the flow is more likely to diffuse towards the outer wall with adverse pressure gradient, which is consistent with the distribution of boundary layer thickness and shear stress shown in Figure 15 and 16.

In addition, negative pressure gradient is formed from the center line of flow towards the outer wall, while the positive pressure gradient is generated towards the inner

wall. As a result, a secondary flow is generated due to the pressure difference between inner and outer wall, of which the direction is same with the pressure gradient (from outer wall to inner wall). Therefore, the secondary flow affects for the motion of the species through the elbow, which is in favor of the mass transport of corrosive species towards the inner wall in a way of convection.

Therefore, it is necessary to investigate the near-wall hydrodynamic parameters as part of the study on corrosion mechanisms, since they can be closely correlated with electrochemical reaction corrosion rates.

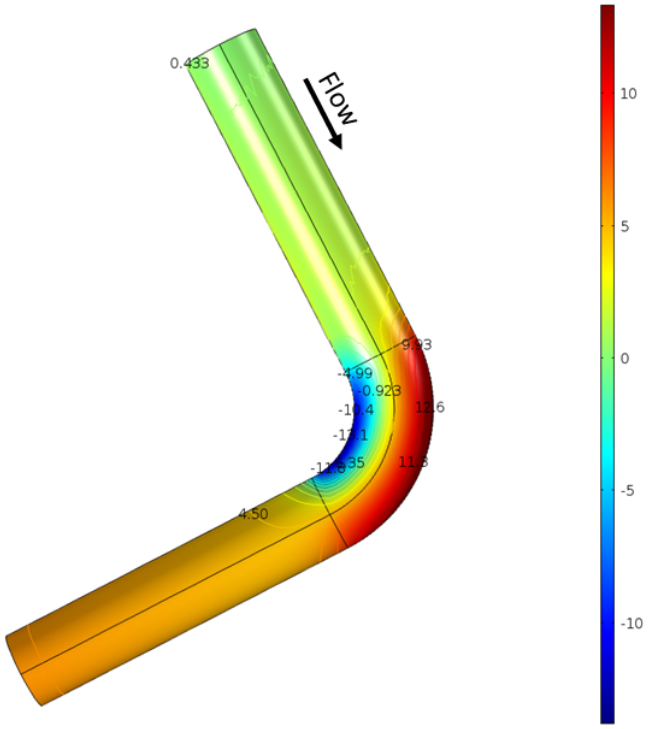

Figure 17. Contours of pressure (Pa) on wall in elbow section

4.2 Corrosion in the pipe and elbow

The comparison of the corrosion rate change between inner wall and outer wall along the flow direction in the pipe and elbow is demonstrated in Figure 18. Corrosion rate keeps identical in the upstream pipe for both inner wall and outer wall until it reaches inlet of the elbow, where corrosion rate at inner and outer wall starts to differentiate. The corrosion rate at inner wall keeps increasing till the peak value at 25^{o} position of elbow. Then the corrosion rate decreases along the outer wall to the lowest value at 90^{o} position (outlet). After exiting from the elbow, the corrosion rate at inner wall increases again in the downstream pipe and gradually reaches constant. In contrast, the corrosion rate at outer wall decreases first at inlet of the elbow till around 10^{o}, then increments in the elbow towards the outlet. The corrosion rate at outer wall in the downstream pipe slightly decreases, but is still higher than the rate on the inner wall. Generally, in the elbow region, corrosion rate on inner wall is larger than outer wall, while in the downstream pipe region, the outer wall has larger corrosion rate.

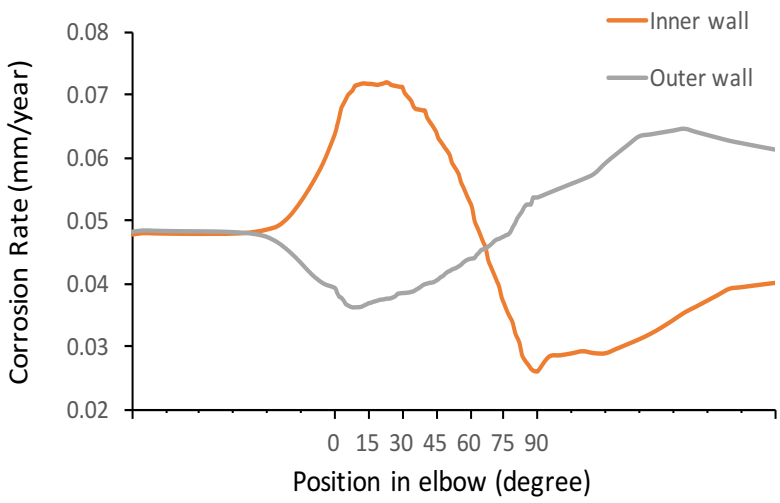

Figure 18. Comparison of corrosion rate between inner wall and outer wall of the pipe and elbow with T=80 ^{o}C, pH=4, 500 ppm CO_2 and 100 ppm H_2S

As shown in Figure 19, the predicted corrosion rate from present model is compared with the measured data from one of the naphtha pipes in ASORC refinery facility and the simulation results from the model by Doheim *et al.*, [44]. The predicted corrosion rate decreases along the inner wall while increases along the outer wall in the direction of flow. This trend is in a good agreement with the measure data in the elbow. The present model's prediction is closer to the measured value as compared with Doheim's model, with the exception that the prediction on the outer wall is slightly lower than the field data. One of the possible explanations for this difference is that, according

to Doheim et al., [43], the pipe in ASORC refinery is also affected by oxygen corrosion, while the present model does not take account for the oxygen corrosion.

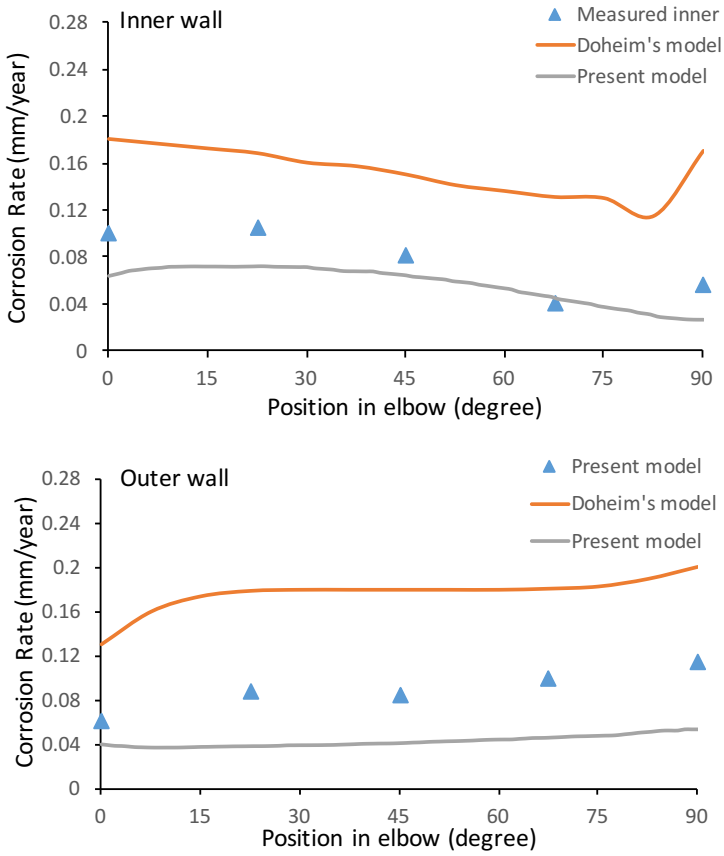

Figure 19. Comparison of present model with the field measurements and published model under the condition of T=80 ^{o}C, pH=4, 500 ppm CO_2 and 100 ppm H_2S. Field data are taken from Doheim et al., [44]

In addition, since the present model is able to calculate the contribution of charge transfer current density to the corrosion rate, which is not accounted in Doheim's model, by coupling the electrochemistry model and mass transport model together, the corrosion rate under the influence of both charge current density and diffusion limit current density

is lower than the one only under the control of diffusion limit current density. From the results of present model, the charge transfer current density of H_2S reduction is within the range of 166 ~ 269 A/m^2. In contrast, as shown in Figure 20, the diffusion limit current density of H_2S is way much smaller, ranging from 8.72×10^{-5} to 1.08×10^{-3} A/m^2. According to $\frac{1}{i_{H_2S}}=\frac{1}{i_{\alpha,H_2S}}+\frac{1}{i^d_{lim,H_2S}}$, it is obvious that the total current density by H_2S is controlled by the diffusion limit current density, so the corrosion rate contributed by H_2S reduction is mass transfer controlled (since corrosion rate is proportional to total current density and diffusion limit current density is proportional to mass transfer coefficient). On the other hand, due to the contribution of charge transfer current density, the total current density of H_2S is small than its diffusion current density (see Figure 20).

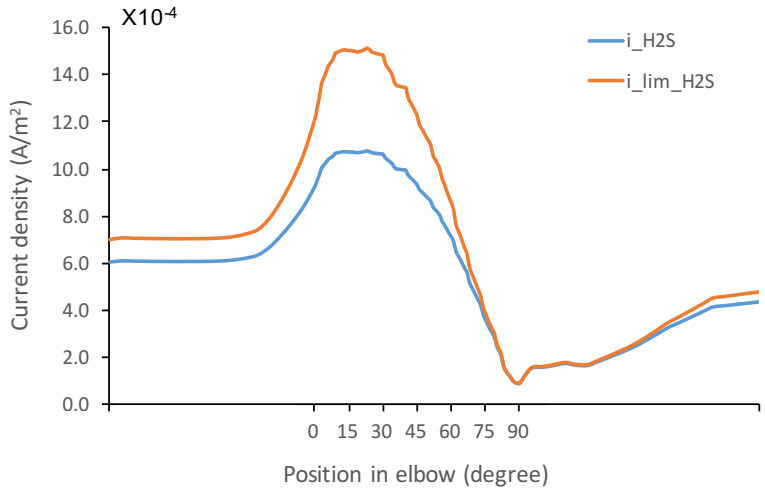

Figure 20. Total current density (i_{H_2S}) and diffusion limit current density (i^d_{lim,H_2S}) of H_2S reduction on inner wall of pipe and elbow under the conditoon of T=80 ^{o}C, pH=4, 500 ppm CO_2 and 100 ppm H_2S

As demonstrated in Figure 21, although the corrosion rate contributed by H^+ reduction is also under mass transfer control, a relatively smaller total current density is obtained as compared to the diffusion limit current density.

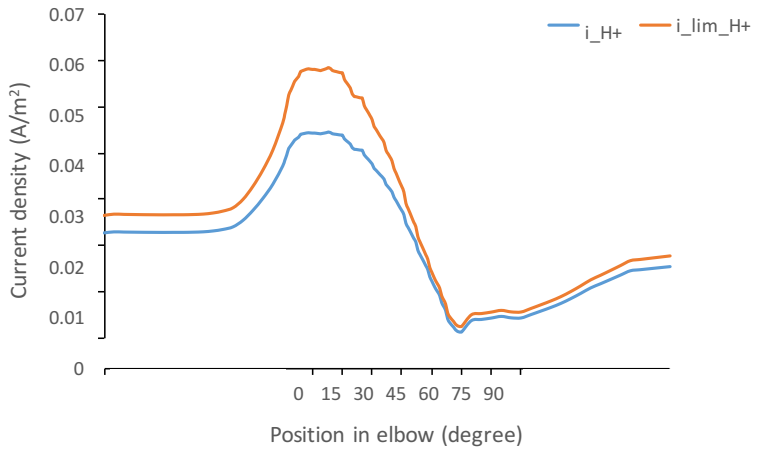

Figure 21. Total current density (i_{H^+}) and diffusion limit current density (i^d_{lim,H^+}) of H^+ reduction on inner wall of pipe and elbow under the condition of T=80 °C, pH=4, 500 ppm CO_2 and 100 ppm H_2S

As for H_2CO_3 reduction, similar trend is observed (see Figure 22), but it needs to be noticed that the total current density is under the control of hydration reaction limit current density (see Equation (73)) instead of mass transfer current density. This is because that the hydration reaction of CO_2 is much slower than the mass transport of H_2CO_3. Since the CO_2 hydration is a function of temperature rather than the flow, the hydration reaction limit current density keeps as a constant throughout the pipe and elbow.

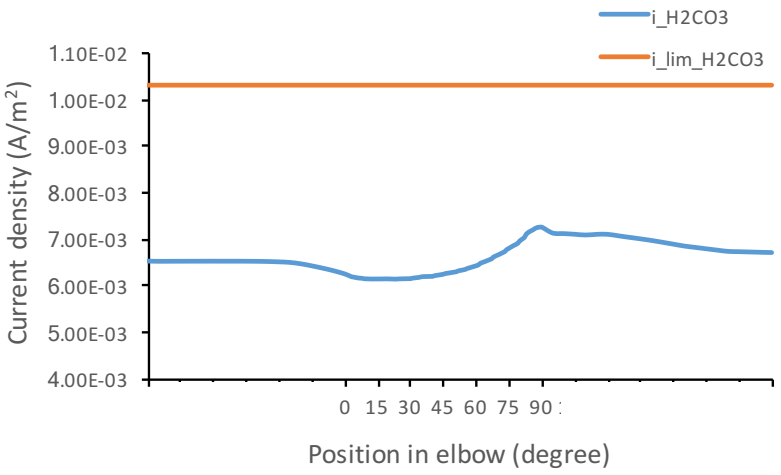

Figure 22. Total current density ($i_{H_2CO_3}$) and hydration limit current density (i^r_{lim,H_2CO_3}) of H_2CO_3 reduction on inner wall of pipe and elbow under the condition of T=80 °C, pH=4, 500 ppm CO_2 and 100 ppm H_2S

Evaluation of corrosion rate in the pipe and elbow under different concentrations of CO_2 and H_2S environment is also conducted by current model. As shown in Figure 23, under the condition of 100 ppm H_2S, an increase in corrosion rate on both inner wall and outer wall is observed as the concentration of CO_2 increased from 10 ppm to 1000 ppm. However, the magnitude of corrosion rate change is not significant, especially for the difference between 10 ppm and 100 ppm CO_2 conditions.

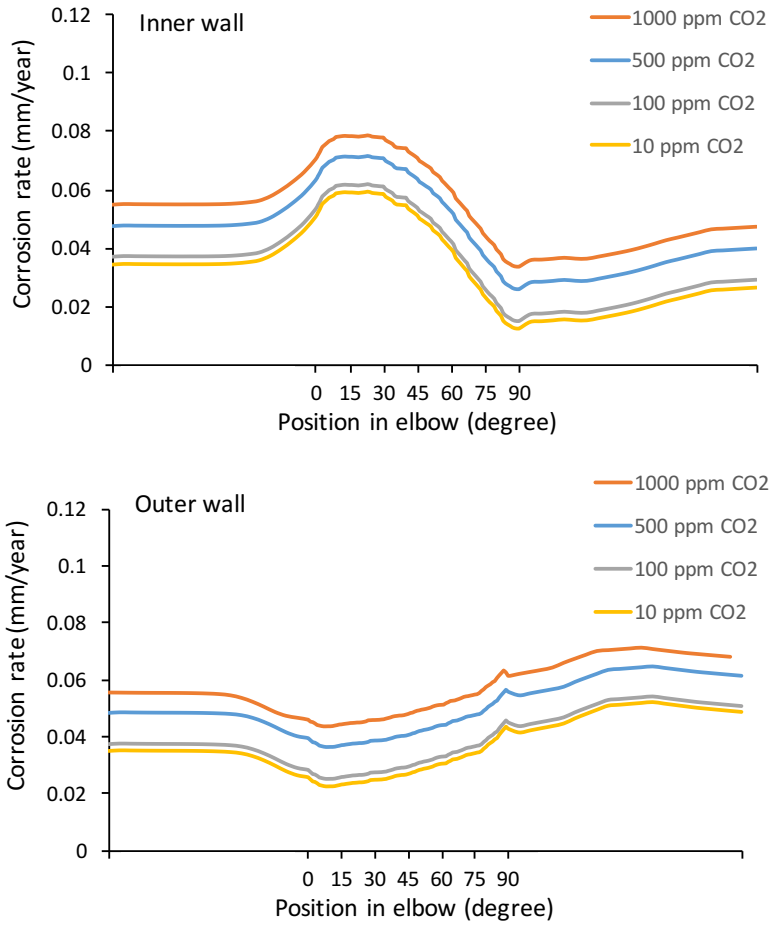

Figure 23. Comparison of corrosion rate in the pipe and elbow under different concentration of CO_2 with the condition of T=80 ^{o}C, pH=4 and 100 ppm H_2S

In contrast, as seen in Figure 24 the corrosion rate under 500 ppm CO_2 environment in the pipe as a function of H_2S concentration, the change of corrosion rate is more sensitive to the change H_2S concentration from 10 ppm to 1000 ppm. The major reason for the difference in sensitivity of corrosion rate to the concentration change is mainly due to slow hydration process of CO_2 to H_2CO_3. For example, for the gas mixture of H_2S and CO_2 with same partial pressure, the concentration of H_2S in aqueous phase is

approximately 1000 times larger than the concentration H_2CO_3 in the aqueous phase. Therefore, in the presence of both H_2S and CO_2, it is more likely that H_2S will dominate the corrosion process.

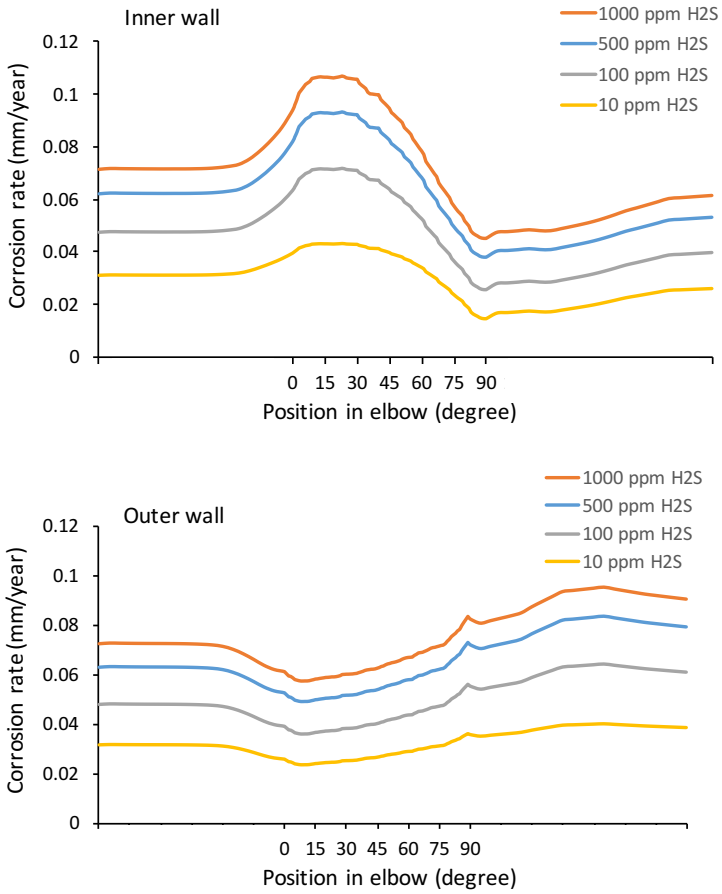

Figure 24. Comparison of corrosion rate in the pipe and elbow under different concentration of H_2S with the condition of T=80 ^oC, pH=4 and 500 ppm CO_2

In order to investigate the effect of temperature on corrosion rate in pipe under the environment in presence of H_2 S and CO_2, simulation is carried out by the present model under different temperature. As seen in Figure 25, corrosion rate calculated from the

model increases by approximately 0.02~0.03 mm/year on both inner wall and outer wall with temperature ramping up from 20 ^{o}C to 80 ^{o}C. In general, temperature is expected to increase the rate chemical reaction and electrochemical reaction, as well as the mass transport process.

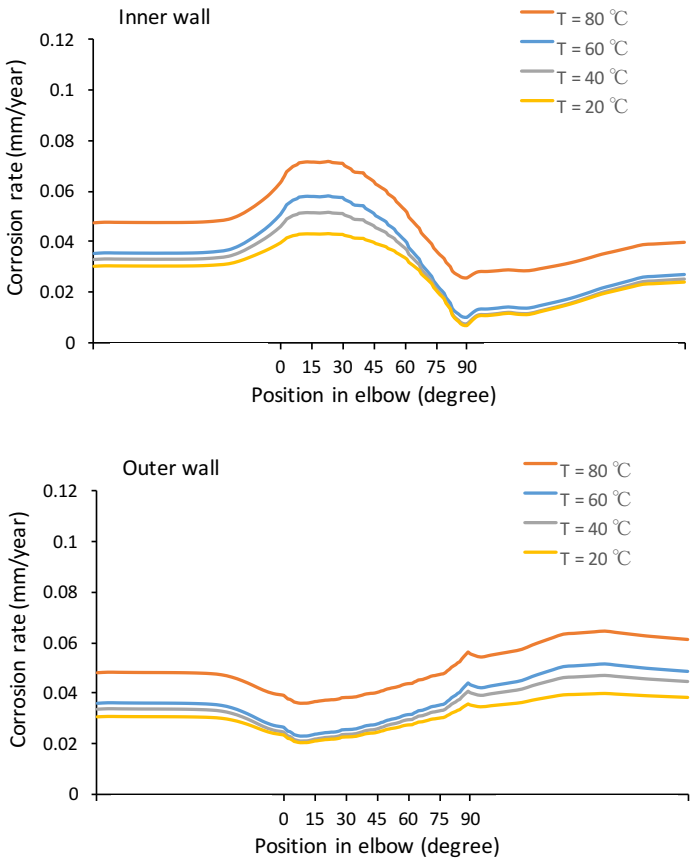

Figure 25. Corrosion rate change in the pipe and elbow as a function of temperature (T=20 ^{o}C, 40 ^{o}C, 60 ^{o}C and 80 ^{o}C) under the condition of pH=4, 500 ppm CO_2 and 100 ppm H_2S

According to Equation (91) and (92), if the supersaturation of FeS (or $FeCO_3$) is larger than 1, protective scale can form.

$$S_{FeS} = \frac{C_{Fe^{2+}} C_{S^{2-}}}{K_{sp\_FeS}} \tag{91}$$

$$S_{FeCO_3} = \frac{C_{Fe^{2+}} C_{CO_3^{2-}}}{K_{sp\_FeCO_3}} \tag{92}$$

Where, K_{sp_FeS} and $K_{sp\_FeCO_3}$ are solubility limit of FeS and FeCO3, respectively, which are both the function of temperature, according to Benning, *et al.*[6], and Sun, *et al.*, [56].

$$K_{sp,FeS} = 10^{\frac{2848.779}{T} - 6.347} K_{hs} K_{bs} \tag{93}$$

$$K_{sp,FeCO_3} = -59.3498 - 0.041377T - \frac{2.1963}{T} + 24.5724 log T \tag{94}$$

As shown in Figure 26, the supersaturation of FeS (S_{FeS}) in the pipe and elbow ranges from 1.2 $\times 10^{-3}$ to 1.6 $\times 10^{-3}$, while the supersaturation of $FeCO_3$ (S_{FeCO_3}) is 1,000 times smaller. This indicates that, under the operation condition of ASORC pipe, both FeS and $FeCO_3$ scales cannot be formed.

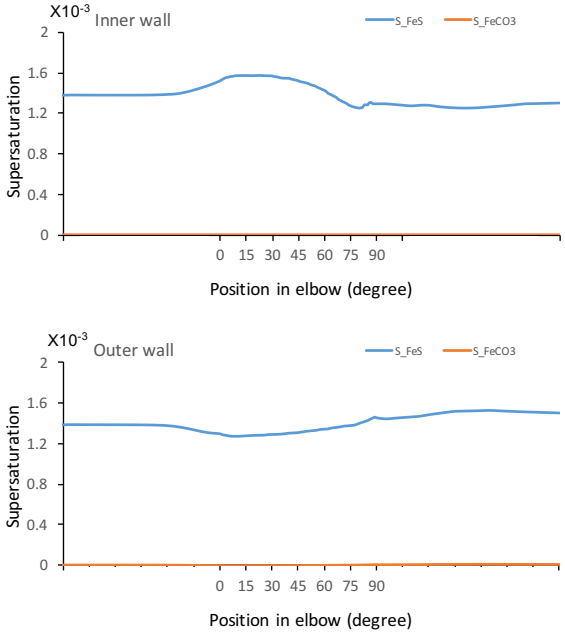

Figure 26. Comparison between the supersaturation of FeS (S_{FeS}) and $FeCO_3$ (S_{FeCO_3}) in the pipe and elbow with the condition of T=80 ^{o}C, pH=4, 500 ppm CO_2 and 100 ppm

CHAPTER V

CONCLUSIONS

An integrated single-phase prediction model for H_2S/CO_2 corrosion in pipe, especially for the case of a 90^o elbow region, has been developed, which is able to solve the four key facets in the corrosion process by incorporating the flow model, the mass transport model and the electrochemistry model:

(1) Flow parameters including wall shear stress, boundary layer thickness and turbulent diffusivity;
(2) Equilibrium reactions and mass transport of corrosive species in boundary layer, which determines the concentration of corrosive species at steel surface;
(3) Current density and corrosion rate, which are proportional to the steel surface concentration and the mass transfer coefficient;
(4) Formation of protective scale based on the concentration of Fe^{2+}, S^{2-} and CO_3^{2-} at steel surface.

The prediction results of present model are compared with the previously published model and the field data of pipeline in an ASORC refinery facility. This model is in good accordance with the measured field data, and follows the prevalent trend of H_2S/CO_2 corrosion process in a pipe and elbow among the existing models. Additionally, it is found in the present model that the charge transfer current density has significant contribution to the corrosion rate, which is ignored in some other models. Apart from that,

other comparisons have been made to investigate the impact on corrosion rate as a function of flow region, H_2S and CO_2 concentration, and temperature. Finally, the present model is able to provide the information on if there are FeS (or $FeCO_3$) protective scales formed at steel surface.

CHAPTER VI

FUTURE WORK

Based on the model in this thesis, some recommendations for future work are listed as follows:

(1) Since pipes in a refinery carry different mixtures of refined products and water, which are normally insoluble with each other in most cases, further study on developing a multi-phase model under different flow patterns, such as stratified flow, slug flow and annular flow, is needed to obtain more accurate prediction results;

(2) The protective scale serves as a diffusion barrier. So further study needs to be conducted to investigate the effect of protective scale on mass transport process by dealing with the thickness and the porosity of scales;

(3) Since there are many other chemicals that can also lead to internal corrosion of a pipe, such as oxygen, ammonia and hydrogen chloride, further study needs to take consideration of more corrosive species existed in the pipe system to generate a more comprehensive prediction result.

REFERENCES

[1] M. Wood, A. Vetere Arellano, and L. Van Wijk, "Corrosion-related accidents in petroleum refineries: lessons learned from accidents in EU and OECD countries," *European Commission Joint Research Centre (JRC), Luxembourg. doi,* vol. 10, p. 379, 2013.

[2] Chemical Safety and Hazard Investment Board, "Chevron Richmond Refinery pipe rupture and fire final investigation report," U.S. Chemical Safety and Hazard Investment Board, 2012-03-I-CA, 2015.

[3] A. Dugstad, "Fundamental aspects of CO_2 metal loss corrosion-part 1: mechanism," in *Corrosion 2006*, 2006: NACE International.

[4] S. Nesic, J. Postlethwaite, and S. Olsen, "An electrochemical model for prediction of corrosion of mild steel in aqueous carbon dioxide solutions," *Corrosion,* vol. 52, no. 4, pp. 280-294, 1996.

[5] S. Nešic and K.-L. Lee, "A mechanistic model for carbon dioxide corrosion of mild steel in the presence of protective iron carbonate films-Part 3: Film growth model," *Corrosion,* vol. 59, no. 7, pp. 616-628, 2003.

[6] M. Nordsveen, S. Nešic, R. Nyborg, and A. Stangeland, "A mechanistic model for carbon dioxide corrosion of mild steel in the presence of protective iron carbonate films-Part 1: Theory and verification," *Corrosion,* vol. 59, no. 5, pp. 443-456, 2003.

[7] G. Schmitt and M. Horstemeier, "Fundamental aspects of CO_2 metal loss corrosion-Part II: Influence of different parameters on CO_2 corrosion mechanisms," in *Corrosion 2006*, 2006: NACE International.

[8] R. Nyborg, "Overview of CO_2 corrosion models for wells and pipes," in *Corrosion 2002*, 2002: Nace International.

[9] C. Morris, *Corrosion Chemistry (Dissolution of iron)*. American Chemical Society, 1979.

[10] X. Cheng, H. Ma, J. Zhang, X. Chen, S. Chen, and H. Yang, "Corrosion of iron in acid solutions with hydrogen sulfide," *Corrosion,* vol. 54, no. 5, pp. 369-376, 1998.

[11] R. H. Hausler, "Contribution to the Understanding of H_2S Corrosion," in *Corrosion 2004*, 2004: NACE International.

[12] D. W. Shoesmith, P. Taylor, M. G. Bailey, and D. G. Owen, "The formation of ferrous monosulfide polymorphs during the corrosion of iron by aqueous hydrogen sulfide at 21 C," *Journal of the Electrochemical Society,* vol. 127, no. 5, pp. 1007-1015, 1980.

[13] S. N. Smith, "A proposed mechanism for corrosion in slightly sour oil and gas production," in *12th International Corrosion Congress, Houston, TX*, 1993.

[14] M. Pourbaix, *Lectures on Electrochemical Corrosion*. New York: Plenum Press, 1973.

[15] J. R. Davis, *Corrosion: Understanding The Basics*. ASM International, 2000.

[16] L. G. Gray, B. G. Anderson, M. J. Danysh, and P. R. Tremaine, "Effect of pH and temperature on the mechanism of carbon steel corrosion by aqueous carbon dioxide," *Corrosion/90, paper,* vol. 40, 1990.

[17] C. De Waard and D. Milliams, "Carbonic acid corrosion of steel," *Corrosion,* vol. 31, no. 5, pp. 177-181, 1975.

[18] J. E. Oddo and M. B. Tomson, "Simplified calculation of $CaCO_3$ saturation at high temperatures and pressures in brine solutions," *Journal of Petroleum Technology,* vol. 34, no. 07, pp. 1,583-1,590, 1982.

[19] D. A. Palmer and R. Van Eldik, "The chemistry of metal carbonato and carbon dioxide complexes," *Chemical Reviews,* vol. 83, no. 6, pp. 651-731, 1983.

[20] Y. K. Kharaka, W. D. Gunter, P. K. Aggarwal, E. H. Perkins, and J. D. DeBraal, "SOLMINEQ. 88: A computer program for geochemical modeling of water-rock interactions," *US Geological Survey Water-Resources Investigation Report,* vol. 88, p. 4227, 1988.

[21] S. Nešić, "Key issues related to modelling of internal corrosion of oil and gas pipes–A review," *Corrosion Science,* vol. 49, no. 12, pp. 4308-4338, 2007.

[22] J. Ning, Y. Zheng, D. Young, B. Brown, and S. Nešic, "Thermodynamic study of hydrogen sulfide corrosion of mild steel," *Corrosion,* vol. 70, no. 4, pp. 375-389, 2013.

[23] O. Suleimenov and R. Krupp, "Solubility of hydrogen sulfide in pure water and in NaCl solutions, from 20 to 320 C and at saturation pressures," *Geochimica et Cosmochimica Acta,* vol. 58, no. 11, pp. 2433-2444, 1994.

[24] J. N. Harb and R. C. Alkire, "Transport and reaction during pitting corrosion of ni in 0.5 m nacl ii. flowing fluid," *Journal of The Electrochemical Society,* vol. 138, no. 12, pp. 3568-3575, 1991.

[25] C. Liu and R. Kelly, "The use of finite element methods (fem) in the modeling of localized corrosion," *The Electrochemical Society Interface,* vol. 23, no. 4, pp. 47-51, 2014.

[26] D. Morris, L. Sampaleanu, and D. Veysey, "The corrosion of steel by aqueous solutions of hydrogen sulfide," *Journal of the Electrochemical Society,* vol. 127, no. 6, pp. 1228-1235, 1980.

[27] R. Galvan-Martinez, J. Mendoza-Flores, R. Duran-Romero, and J. Genesca-Llongueras, "Effects of turbulent flow on the corrosion kinetics of X 52 pipe steel in aqueous solutions containing H 2 S," *Materials and Corrosion,* vol. 55, no. 8, pp. 586-593, 2004.

[28] W. Sun *et al.*, "Laboratory study of sour localized/pitting corrosion," in *Corrosion 2011*, 2011: NACE International.

[29] J. Kvarekval, A. Dugstad, I. H. Omar, and Y. Gunaltun, "H_2S corrosion of carbon steel under simulated kashagan field conditions," in *Corrosion 2005*, 2005: NACE International.

[30] M. R. Bonis, M. Girgis, K. Goerz, and R. MacDonald, "Weight loss corrosion with H2S: using past operations for designing future facilities," in *Corrosion 2006*, 2006: NACE International.

[31] C. Canto, B. Brown, and S. Nesic, "Integrity of corrosion inhibitor films in multiphase flow," *NACE Corrosion/11, paper,* no. 238, 2011.

[32] S. Turgoose, R. Cottis, and K. Lawson, "Modeling of electrode processes and surface chemistry in carbon dioxide containing solutions," in *Computer Modeling in Corrosion*: *ASTM International*, 1992.

[33] M. Sundaram, V. Raman, M. High, D. Tree, and J. Wagner, "Deterministic modeling of corrosion in downhole environments," *NACE International, Houston, TX (United States)*, 1996.

[34] E. Dayalan, F. De Moraes, J. R. Shadley, E. F. Rybicki, and S. A. Shirazi, "CO_2 corrosion prediction in pipe flow under $FeCO_3$ scale-forming conditions," in *Corrosion 98*, 1998 *: Nace International*.

[35] S. Nesic, M. Nordsveen, and A. Stangel, "A mechanistic model for co_2 corrosion with protective iron carbonate films," in *Corrosion 2003*, 2003: Nace International. 2003.

[36] S. Nešić, M. Nordsveen, R. Nyborg, and A. Stangeland, "A diffusion-based model for uniform corrosion," in *Defect and Diffusion Forum*, 2001, vol. 194, pp. 1661-1674: Trans Tech Publ.

[37] Y. Zheng, J. Ning, B. Brown, and S. Nešić, "Advancement in predictive modeling of mild steel corrosion in CO_2 and H_2S containing environments," *Corrosion,* vol. 72, no. 5, pp. 679-691, 2016.

[38] T. Tan, Y. Chen, and H. Chen, "Theoretical modeling and numerical simulation of the corrosion and precipitation in non-isothermal liquid lead alloy pipe/loop systems," *Heat and Mass Transfer,* vol. 44, no. 3, pp. 355-366, 2008.

[39] J. Zhang and N. Li, "Parametric study of a corrosion model applied to lead–bismuth flow systems," *Journal of Nuclear Materials,* vol. 321, no. 2, pp. 184-191, 2003.

[40] J. Liu, Y. Lin, and X. Li, "Application of numerical simulation to flow-induced corrosion in flowing seawater systems," *Anti-Corrosion Methods and Materials,* vol. 52, no. 5, pp. 276-279, 2005.

[41] K. Das, D. Basu, and T. Mintz, "Comparative assessment of turbulence models for prediction of flow-induced corrosion damages," in *ASME 2011 Pressure Vessels and Piping Conference*, 2011, pp. 51-60: American Society of Mechanical Engineers.

[42] Y. Cui, H.-Q. Lan, Z.-L. Kang, R.-Y. He, H. Huang, and N. Lin, "Updated CO_2/H_2S internal corrosion model of natural gas pipes based on flow field calculations," *Corrosion Engineering, Science and Technology,* vol. 49, no. 1, pp. 39-44, 2014.

[43] M. A. Doheim, H. M. Elbatsh, and A. F. Hassan, "Prediction for the mass transfer and oxygen corrosion in complex pipes," *Proceedings of ICFD,* vol. 9, pp. 18-21.

[44] M. A. Doheim, H. M. El-Batsh, and A. F. Hassan, "Prediction of hydrogen sulfide corrosion in petroleum refinery complex pipes," *Proceedings of ICFD,* vol. 10, pp. 16-19, 2010.

[45] I. Bockris, "'M. The electrode kinetics of the deposition of iron/I. O'M. Bockris, D. Drazic, AR Despic," *Electrochimica Acta,* vol. 4, pp. 325-361, 1961.

[46] Y. Zheng, B. Brown, and S. Nešić, "Electrochemical study and modeling of H_2S corrosion of mild steel," *Corrosion,* vol. 70, no. 4, pp. 351-365, 2013.

[47] K. Videm and J. Kvarekvål, "Corrosion of carbon steel in carbon dioxide-saturated solutions containing small amounts of hydrogen sulfide," *Corrosion,* vol. 51, no. 4, pp. 260-269, 1995.

[48] Y. Zheng, J. Ning, B. Brown, and S. Nešić, "Electrochemical model of mild steel corrosion in a mixed H_2S/CO_2 aqueous environment in the absence of protective corrosion product layers," *Corrosion,* vol. 71, no. 3, pp. 316-325, 2014.

[49] J. S. Newman, *Electrochemical Systems, 2nd ed*. NJ: Prentice Hall: Englewood Cliffs, 1991.

[50] D. G. R.H. Perry, *Perry's Chemical Engineers' Handbook, 50th ed*. New York, NY: McGraw-Hill, 1984.

[51] J. Kvarekvål, "A kinetic model for calculating concentration profiles and fluxes of CO_2 related species across the Nernst diffusion layer," *NACE International, Houston, TX (United States)*, 1997.

[52] J. T. Davies, *Turbulence Phenomena*. London, U.K.: Academic Press, 1992.

[53] Y. A. Cengel, *Fluid Mechanics*. Tata McGraw-Hill Education, 2010.

[54] L. Jingjun, L. Yuzhen, and L. Xiaoyu, "Numerical simulation for carbon steel flow-induced corrosion in high-velocity flow seawater," *Anti-Corrosion Methods and Materials,* vol. 55, no. 2, pp. 66-72, 2008.

[55] H. Rani, T. Divya, R. Sahaya, V. Kain, and D. Barua, "Unsteady turbulent flow in 90° bend under the wall thinning degradation environment," *Nuclear Engineering and Design,* vol. 267, pp. 164-171, 2014.

[56] E. Lamy-Pitara and J. Barbier, "The electrocatalytic reactions of oxidation and evolution of hydrogen on iridium electrodes modified by sulphur adsorption," *Journal of Electroanalytical Chemistry,* vol. 416, no. 1-2, pp. 47-51, 1996.